

A GNSS velocity field for crustal deformation studies: The influence of glacial isostatic adjustment on plate motion models

Katarina Vardić ¹, Peter J. Clarke ¹ and Pippa L. Whitehouse ²

¹School of Engineering, Newcastle University, Newcastle upon Tyne, NE17RU, UK, E-mail: kv.ncl@runbox.com.

²Department of Geography, Durham University, Durham DH13LE, UK

Accepted 2022 February 2. Received 2022 January 30; in original form 2021 August 8

SUMMARY

The two main causes of global-scale secular deformation of the Earth are tectonic plate motion and glacial isostatic adjustment (GIA). We create a bespoke global 3D GNSS surface velocity field ‘NCL20’ to investigate tectonic plate motion and the effect of GIA on plate motion models (PMMs), drawing on a set of 1D and 3D GIA model predictions. The main motivation for creating NCL20 is to include a larger number of GNSS sites in the most GIA-affected areas of investigation, namely North America, Europe, and Antarctica. We do this using the IGS repro2 data and other similarly processed GNSS data sets. Our final GNSS velocity field has horizontal uncertainties mostly within $\pm 0.5 \text{ mm yr}^{-1}$ and vertical uncertainties mostly within $\pm 1 \text{ mm yr}^{-1}$ (at 95 per cent confidence), which make it suitable for testing GIA models. We generate a suite of 117 global GIA model predictions by combining three different ice history models (ICE-5G, ICE-6G and W12) with a range of 1D and 3D Earth models. By subtracting this ensemble from the GNSS velocity field, we identify and compare a range of PMMs which are expected to be unaffected by GIA. Our method allows us to include GNSS sites that are typically excluded from PMM estimations due to their location in GIA-affected regions. We demonstrate that significant GIA-related horizontal motion outside of the rapidly uplifting regions may bias PMMs if left uncorrected. Based on their ability to explain the observed surface velocity field, a group of best-performing GIA models is selected for three regions of interest: North America, Europe and Antarctica. The range of GIA predictions in each best-performing group is assumed to represent the uncertainty in regional GIA modelling insofar as it can be constrained by present-day geodetic velocities. In the horizontal component, we note that 3D GIA models show more variation in the direction of predicted velocities than 1D GIA models, confirming that horizontal velocities are strongly sensitive to lateral variations in Earth structure. Furthermore, for Antarctica the variation in predicted GIA vertical velocities suggests that the total GIA contribution to annual gravimetric mass change ranges from -3 to 22 Gt yr^{-1} depending on which of the best-performing GIA models is used.

Key words: Plate motions; Reference systems; Satellite geodesy; Time-series analysis; Intraplate processes.

1 INTRODUCTION

Globally, the dominant secular processes causing surface deformation are tectonic plate motion and glacial isostatic adjustment (GIA; defined here as the response of the solid Earth to past ice and ocean surface mass load change, Karato 2008). Quantifying and modelling crustal deformation at local to global scales improves our understanding of the underlying processes, for example seismic activity, polar motion and tectonics (Lowrie 2007). The advent of space geodesy has contributed substantially to studies of crustal deformation (Bock & Melgar 2016).

A measurement can only be as accurate as the realization of the coordinate system it is expressed in. Consequently, a high-quality terrestrial reference frame is crucial for constraining processes such as GIA and plate tectonics that take place on the millimetre/year scale (Plag & Pearlman 2009). Global space-geodetic networks provide geocentric site coordinates for specific epochs as well as site velocities. Individual network solutions are combined to form the integral part of the International Terrestrial Reference Frame (ITRF). ITRF2014 (Altamimi *et al.* 2016) is the most recent ITRF. Besides using a longer time-span of measurements than the previous ITRFs, ITRF2014 incorporates data from the International GNSS

Service (IGS) second reprocessing campaign (repro2), a full re-analysis of GNSS data collected since 1994, which provides a more extensive and accurate data set of surface velocities than previously. ITRF2014 takes into consideration annual and semi-annual signals as well as providing post-seismic deformation models for sites affected by earthquakes. It is therefore the most accurate ITRF to date.

Horizontal velocities derived from global space-geodetic networks mainly reflect tectonic plate motion (Torge & Müller 2012). The earliest plate motion models (PMMs), such as those developed by Chase (1978) and Minster & Jordan (1978), used geophysical and geological data. Other models based on geological/geophysical data include NUVEL-1 (DeMets *et al.* 1990) and its updated version NUVEL-1A (DeMets *et al.* 1994), PB2002 (Bird 2003) and MORVEL (DeMets *et al.* 2010), and they use, for example ocean floor magnetic anomalies, transform fault azimuths, earthquake slip vectors, to estimate the motion of the plates (Bastos *et al.* 2010). More recently, the development of space-geodetic techniques and systems has made it possible to construct PMMs from geodetic observations alone (e.g. Larson *et al.* 1997; Lavallée 2000; Argus *et al.* 2010; Altamimi *et al.* 2012, 2017; Booker *et al.* 2014).

Geodetic plate motion models (PMMs) describe the motion of a set of rigid plates rotating on Earth's surface. It is assumed that the plates are capable of transmitting stresses over long horizontal distances without distorting and that relative motion between plates is taken up only along plate boundaries (Fowler 2005). Therefore, observations of horizontal motion corrected for plate motion should allow testing of whether tectonic plates are rigid, assuming no other large-scale processes are operating. However, in current and former glaciated regions, GIA causes long wavelength vertical and horizontal movement of Earth's surface, which must be accounted for when investigating plate rigidity. Models of GIA are typically tuned to fit evidence for past vertical motion, as determined from historical relative sea level data (e.g. Whitehouse 2009), and they may additionally be tuned to fit GNSS-derived present-day vertical rates (e.g. Peltier *et al.* 2015). Recently, Coulson *et al.* (2021) have highlighted the importance of considering the horizontal GNSS velocity field when studying the solid Earth response to surface mass change. They quantify the signal associated with contemporary mass change, which we account for when we assess GNSS velocities across Antarctica, but our primary focus is on the horizontal GIA signal, which is typically an order of magnitude greater than the signal studied by Coulson *et al.* (2021). GNSS-derived horizontal rates have not traditionally been used to tune GIA models, primarily because the presence of lateral Earth structure is known to significantly influence horizontal GIA rates (Kaufmann *et al.* 2005). Most GIA models (so-called 1D GIA models) do not account for lateral Earth structure, but the recent development of GIA models that do (so-called 3D GIA models) opens up the possibility of using GNSS-derived horizontal velocities to provide novel insight into GIA.

Horizontal GIA motion can be partially absorbed into a plate-fixed regional reference frame or PMMs determined from space-geodetic techniques (Plag *et al.* 2002; Kierulf *et al.* 2003), resulting in inaccurate regional reference frames or PMMs. Métivier *et al.* (2020) compare vertical GNSS velocities from different ITRF realizations with a set of recent 1D GIA models, but refrain from analysing the horizontal velocities due to possible contamination of the plate motion models by insufficiently known GIA signals. King *et al.* (2015) conclude that regardless of the fact that the horizontal GIA signal is usually small compared to plate motion, not considering GIA when estimating plate motion may introduce biases. This

supports the conclusions of Kleemann *et al.* (2008), who find that the magnitude of the GIA signal is sufficient to influence the accuracy of the plate motions determined by precise GNSS observations.

The issue of how to account for GIA-related horizontal deformation when constructing PMMs poses a significant challenge. The ITRF2008 plate motion model (ITRF2008 PMM, Altamimi *et al.* 2012) is a geodetic plate motion model aligned to the ITRF2008 reference frame (Altamimi *et al.* 2011). In creating the ITRF2008 PMM, Altamimi *et al.* (2012) attempted to correct the network velocities for GIA before estimating plate models by using GIA model output from Schotman & Vermeersen (2005), who combined the ICE-5G ice model with Earth models VM2 and VM4 (Peltier 2004). Corrections were applied to the three plates most affected by GIA: Antarctic, Eurasian and North American. However, Altamimi *et al.* (2012) concluded that using these GIA models did not significantly improve the fit of the PMM to the observed velocities and consequently, no GIA correction was applied when producing the final ITRF2008 PMM. The ITRF2014 PMM is a successor to the ITRF2008 PMM, consistent with the ITRF2014 reference frame (Altamimi *et al.* 2017). Similarly to the ITRF2008 PMM, no GIA correction was applied, and instead sites used for PMM estimation were chosen based on several criteria, one of which was that they must be located far from GIA-affected regions. Altamimi *et al.* (2017) satisfy this condition by excluding sites with vertical GIA velocities $\geq 0.75 \text{ mm yr}^{-1}$, as predicted by the Australian National University GIA model of Lambeck *et al.* (2014, 2017). Sites in Antarctica were retained regardless of this condition, in order to be able to estimate Antarctic plate motion and because their tests suggested that the Euler pole of the Antarctic plate could only marginally be biased by GIA effects. Altamimi *et al.* (2017) did not use predictions of GIA-related horizontal motion to select which sites would be excluded, but state that far from GIA regions, horizontal velocities due to GIA of up to $3\text{--}4 \text{ mm yr}^{-1}$ may be found.

In this paper, we create a bespoke GNSS velocity field 'NCL20' and use it in combination with GIA model predictions to estimate PMMs. Unlike the ITRF PMM approach, we do not exclude sites in GIA regions but instead use GIA model predictions to mitigate the influence of GIA on the PMM estimate. A similar approach was taken by Booker *et al.* (2014) who created a global GNSS velocity field from IGS repro1 GNSS solutions and corrected it using two 1D GIA models before estimating plate motion. We use a much larger suite of GIA models than either Booker *et al.* (2014) or Altamimi *et al.* (2012), and include 3D GIA models. GIA vertical motion is expected to be greatest in the centre of the former ice sheets, whereas the largest horizontal velocities are expected in peripheral bulge regions (King *et al.* 2010). An approach that excludes sites in the area of large vertical velocities might introduce bias by retaining sites in peripheral bulge regions that have small GIA-related vertical velocities but relatively large GIA-related horizontal velocities. The difficulty of defining robust criteria to identify sites affected by GIA motivates our approach. Our rigorous consideration of horizontal motion due to GIA should improve the estimation of PMMs.

The primary aim of our study is to investigate the effect of GIA on a PMM estimate. A secondary aim is to identify the suite of GIA model predictions that minimizes the magnitude of the residual velocity field, that is, the velocity field that remains after subtracting a GIA model and its respective PMM from NCL20. Our GNSS surface velocity field and PMMs are global but we focus additionally on three regions affected by GIA—Europe, North America and Antarctica. Antarctica is still largely covered with ice sheets and therefore, in addition to GIA effects, there we account for the elastic response to present-day ice mass changes.

In Section 2, we present the data sets used in this paper, the GNSS daily position networks, and the set of 1D and 3D models used to estimate GIA. Section 3 and Appendix A describe the methodology of combining GNSS networks, obtaining the velocity field from time series of daily position networks, and refinements to the velocity field. Further, Section 3 provides the method for creating the geodetic PMMs and computing the residual velocity field. In Section 4, we present our results, including the NCL20 GNSS velocity field and the comparison of PMMs created using a range of 1D and 3D GIA models. In Section 4.1, we present and compare the PMMs. In Section 4.2, we investigate the range of GIA model predictions that are compatible with NCL20, and assess the fit of the models to the plate-motion-corrected GNSS velocity field, focusing on horizontal GIA velocities. In Sections 5 and 6, we discuss and conclude our results, respectively.

2 DATA SETS

2.1 Input GNSS solutions

We created a global GNSS network solution by combining epoch solutions from global and regional Analysis Centres (ACs). These solutions are published as daily site coordinate network solutions which include site position coordinates with their standard deviations and the correlations between sites and coordinate components. The global and regional solutions are listed in Fig. A1. Solutions COD, EMR, ESA, GFZ, GRG, JPL, MIT and SIO are global solutions provided by the IGS ACs, see Table A1. NMT (North America) and ANT (Antarctica) are regional solutions provided by New Mexico Tech as part of the Plate Boundary Observation project ([ftp://data-out.unavco.org/pub/products/sinex/](http://data-out.unavco.org/pub/products/sinex/)). The Fennoscandian and Baltic regional solutions, denoted as BAL (Baltic), FIN (Finland), NOR (Norway) and SWE (Sweden), were provided by Halfdan P. Kierulf [personal communication (2019) and Kierulf *et al.* (2021)]. The EUREF (European Permanent GNSS Network, <http://www.epnccb.oma.be/>) provides regional solutions for Europe (EUR).

2.2 GIA models

We generated a suite of GIA model predictions by combining three different ice models, ICE-5G (Peltier 2004), ICE-6G (Peltier *et al.* 2015) and W12 (Whitehouse *et al.* 2012), with a range of 1D and 3D Earth models. Model predictions are referred to as ‘1D’ or ‘3D’, depending on the type of Earth model used.

The 1D GIA model predictions were produced using a model that solves the sea-level equation using the approach outlined in Mitrovica *et al.* (2001); Mitrovica & Milne (2003); Kendall *et al.* (2005). The model accounts for rotational feedback and shoreline migration. The Earth models in the 1D case assume a spherically symmetric, self-gravitating Earth with an elastic lithosphere of uniform thickness and a viscoelastic mantle with linear viscosity. The elastic structure is given by the Preliminary Reference Earth Model (PREM, Dziewonski & Anderson 1981). We use three different values of lithosphere thickness: 71 km, 96 km and 120 km. The mantle is divided into the upper and lower mantle. Choices for upper mantle viscosity, η_{UM} , are 0.3×10^{21} Pa s, 0.5×10^{21} Pa s or 0.8×10^{21} Pa s and choices for lower mantle viscosity, η_{LM} , are 5×10^{21} Pa s, 10×10^{21} Pa s or 20×10^{21} Pa s. Combining these parameter choices with the three ice models yields 81 different 1D GIA model

predictions. We use a model-naming convention that reflects the ice model, lithosphere thickness and upper and lower mantle viscosity (quoted as a multiple of 10^{21} Pa s, with ‘p’ representing a decimal point) used to generate the model prediction, for example a combination of ICE-5G with 120 km lithosphere thickness, 0.5×10^{21} Pa s η_{UM} and 10×10^{21} Pa s η_{LM} is denoted as 5G_120p510.

A finite element approach was used to generate the 3D GIA model predictions, as described in van der Wal *et al.* (2013). The approach does not account for rotational feedback, which generates a long wavelength signal that would be similar for all models tested here due to our use of a common viscosity profile below 400 km (King *et al.* 2015). The coherence of the rotational feedback signal on small spatial scales means that it may be mistaken for plate motion if not robustly accounted for, but the small magnitude of the signal (up to ~ 0.5 mm yr $^{-1}$; Mitrovica *et al.* 2001) means that it will have a relatively minor effect on our PMM solutions. For the largest plates, failure to accurately account for rotational feedback may lead to a component of intraplate deformation being retained in the velocity field, which makes it more challenging to fit a plate model. The horizontal resolution of our global finite element grid is 2° . We do not account for plate boundaries and, beneath a 35-km-thick elastic crust, five layers of elements represent the lithosphere and upper mantle: 35–70 km, 70–120 km, 120–170 km, 170–230 km and 230–400 km, with lithospheric behaviour implied by the material properties defined in relevant elements. Unlike the 1D GIA model described above, which assumes linear (Newtonian) rheology, our 3D GIA model adopts a non-linear, power law rheology in which effective viscosity depends on stress, reflecting the results of laboratory deformation experiments designed to investigate stress-strain-rate relations in the mantle (Karato 2008). In addition to stress, effective viscosity depends on the composition, grain size, water content and temperature of the mantle (Hirth & Kohlstedt 2003). All our elements are assumed to have the same chemical composition, we use global grain sizes of 1, 4 and 10 mm, and mantle water content is varied globally between a wet (1000 ppm H₂O) and a dry state. These properties likely vary with depth and laterally, but further work is needed to understand how to assign 3D variations on a global scale. Previous work (van der Wal *et al.* 2013) suggests the global values we adopt sufficiently cover the parameter space. Within our 3D GIA model, spatial variations in viscosity arise due to spatial variations in stress (in response to surface loading) and the fact that we assign a different temperature value to each element of the finite element grid. These temperature variations are derived from seismic velocity models SL (Schaeffer & Lebedev 2013) and S40RTS (Ritsema *et al.* 2011) following the methods in van der Wal *et al.* (2013). Below 400 km, a 1D temperature profile is adopted, reflecting the decreased amplitude of seismic velocity anomalies at greater depths and the lower sensitivity of regional GIA model predictions to the details of viscosity at these depths. Combining our parameter choices with the three ice models yields 36 different 3D GIA model predictions. We use a naming convention that reflects the ice model, seismic velocity model, water content and grain size used to generate the model prediction, for example 6G_S_wet_10mm (we use ‘S’ to refer to the S40RTS model).

Due to the different approaches used to define the 1D and 3D Earth models, it is not straightforward to identify matching properties of 1D and 3D GIA models. Within the 3D models, lower viscosities are typically associated with a smaller grain size, higher mantle temperature or higher mantle water content while higher viscosities are associated with a larger grain size, lower mantle temperature, or lower mantle water content.

The 1D and 3D GIA models described above are not expressed in the same reference frame, which we take into consideration when estimating the PMMs (Section 3.2) and computing the residual velocity field (Section 3.3). The 1D models are expressed in the centre of mass of the solid Earth [CE, see e.g. Blewitt (2003)] and the 3D models are expressed in a reference frame with its origin at the centre of mass of the finite element model, which we denote CFEM. In addition, the 1D models are compressible whereas the 3D models are incompressible. Neglecting compressibility in the 3D models will lead to small biases in the estimation of horizontal velocities in both the near and far field (Tanaka *et al.* 2011). However, this does not affect our overall conclusions because our aim is to explore the parameter space of GIA model predictions as widely as possible, in order to better understand the likely impact of GIA on PMMs.

Three independent ice models were used to generate the GIA model predictions. ICE-5G and ICE-6G are global ice models from the ICE-x series that have been developed for use within GIA models. The ICE-x models are based on dated observations of ice-sheet margins and records of past sea level. ICE-5G was developed in conjunction with the VM2 (viscosity model 2) Earth model, resulting in the GIA model ICE-5G VM2 (Peltier 2004). ICE-6G was developed in conjunction with the VM5a Earth model, resulting in the ICE-6G_C (VM5a) GIA model (Peltier *et al.* 2015). Radial viscosity profiles VM2 and VM5a are similar, but VM2 has a greater number of layers. It should be noted that ICE-5G and ICE-6G were tuned in conjunction with their respective Earth models to fit vertical GPS measurements and records of past sea-level change, i.e. they were developed assuming a 1D Earth model. W12 (Whitehouse *et al.* 2012) is a model of ice sheet history for Antarctica which is combined with the northern hemisphere component of ICE-5G for the purpose of generating global GIA predictions. Unlike the ICE-x series, the W12 ice sheet history for Antarctica was not tuned by seeking to fit observations that jointly depend on ice history and Earth rheology. Instead, it was tuned to fit an extensive data base of geological and glaciological data relating to past ice extent, with the overall geometry of the ice sheet determined using a numerical ice sheet model.

3 METHODOLOGY

We start from the assumption that observed motion at GNSS sites consists of rigid plate motion, GIA-induced motion and other lesser present-day motions (e.g. due to local tectonics, hydrology, recent or contemporary ice melt—the latter is accounted for at Antarctic sites) which we denote residual secular motion, that is:

$$\dot{X} = \dot{X}_{\text{plate,motion}} + \dot{X}_{\text{GIA}} + \dot{X}_{\text{residual}}. \quad (1)$$

In order to calculate PMMs that take GIA into account, we created a GNSS surface velocity field (Appendix A) and removed a suite of GIA model predictions. The resulting velocity fields were used to determine a suite of plate motion models. Fig. 1 summarises our method.

3.1 Creating the GNSS velocity field

The GNSS epoch solutions (*cf.* Section 2.1) are combined and aligned to the final reference frame on a daily level. For each day in the time series, we combined multiple global epoch solutions (Table A1 and Fig. A1 - top) into a unique (combined) global epoch solution of high stability. We aligned each combined global daily solution to the most recent ITRF2014 reference frame. Additionally, several regional network solutions (Fig. A1 - bottom) were aligned

to the unique global solutions (*cf.* Section A2.2). The GNSS solutions we used were processed with the latest available methods and models at the time: all the global and regional solutions adhere to IGS repro2 standards. Every network solution gives standard deviations of site position coordinates and the correlations between the network sites. Throughout the network combination and alignment process, we detect and handle outliers using the Tanya software (Davies & Blewitt 2000; Lavallée 2000; Booker *et al.* 2014). Tanya is a reference frame combination software (see Section A2) which we updated to facilitate changes in the network combination method and ITRF. The described process has been carried out for each day in the time series (from year 1996 to 2017, i.e. from GPS week 900 to 1933). Finally, the resulting time series of GNSS position coordinates in a united reference frame was used to estimate linear velocities (Section A3). The sites selected through multiple steps of quality control constitute the final GNSS surface velocity field which we denote NCL20. The details of creating the velocity field are presented in Appendix A.

3.2 Plate motion model estimation

3.2.1 Mathematical model

The motion of the (rigid) plates on the Earth is described by Euler's rotation theorem. In geocentric Cartesian coordinates, an Euler pole and its rotation rate are defined by a 3×1 vector known as the Euler vector. The Euler vector $\Omega_p = [\omega_x \ \omega_y \ \omega_z]^T$ of a plate p is

$$\Omega_p = \omega_p e_p, \quad (2)$$

where ω_p is the rotation rate and e_p is the unit vector along the Euler pole's rotation axis.

The plate velocity \dot{X}_i of a site at position X_i on plate p with rotation described by the absolute Euler vector Ω_p is given by:

$$\dot{X}_i = \Omega_p \times X_i, \quad (3)$$

A plate motion model (PMM) can be estimated using least-squares adjustment from observed site velocities. When estimating all Euler vectors together from a global velocity field (i.e. estimating a global PMM), we build on the following functional model:

$$\dot{X}^{\text{obs}} = \Omega \times X + v, \quad (4)$$

where X and \dot{X}^{obs} are the vectors of site positions and observed site velocities, respectively, and Ω contains Euler vectors for all plates in the estimation (those which have enough GNSS sites). Vector v represents the residuals of the PMM estimation. The GNSS velocity field we have created is aligned to the ITRF2014 reference frame (Section A2.2), thus satisfying the No-Net-Rotation (NNR) condition and allowing us to estimate an absolute PMM in this reference frame. PMM estimation and outlier detection was carried out using geocentric Cartesian coordinates, expressing velocities and PMMs in the ITRF2014 reference frame. Hence, when estimating a global PMM from velocities on multiple plates it was possible to estimate the translational velocity vector of the centre around which the plates rotate with respect to the geocentre of the ITRF2014-aligned GNSS velocity field. We denote this vector as 'geocentre origin rate bias' β , in accordance with Altamimi *et al.* (2017), and extend our functional model as follows:

$$\dot{X}^{\text{obs}} = \Omega \times X + \beta + v. \quad (5)$$

Eq. (5) describes the plate motion model that is estimated if no correction is made for GIA. We refer to this as the GNSS-only PMM. However, we also seek to estimate PMMs that are unaffected

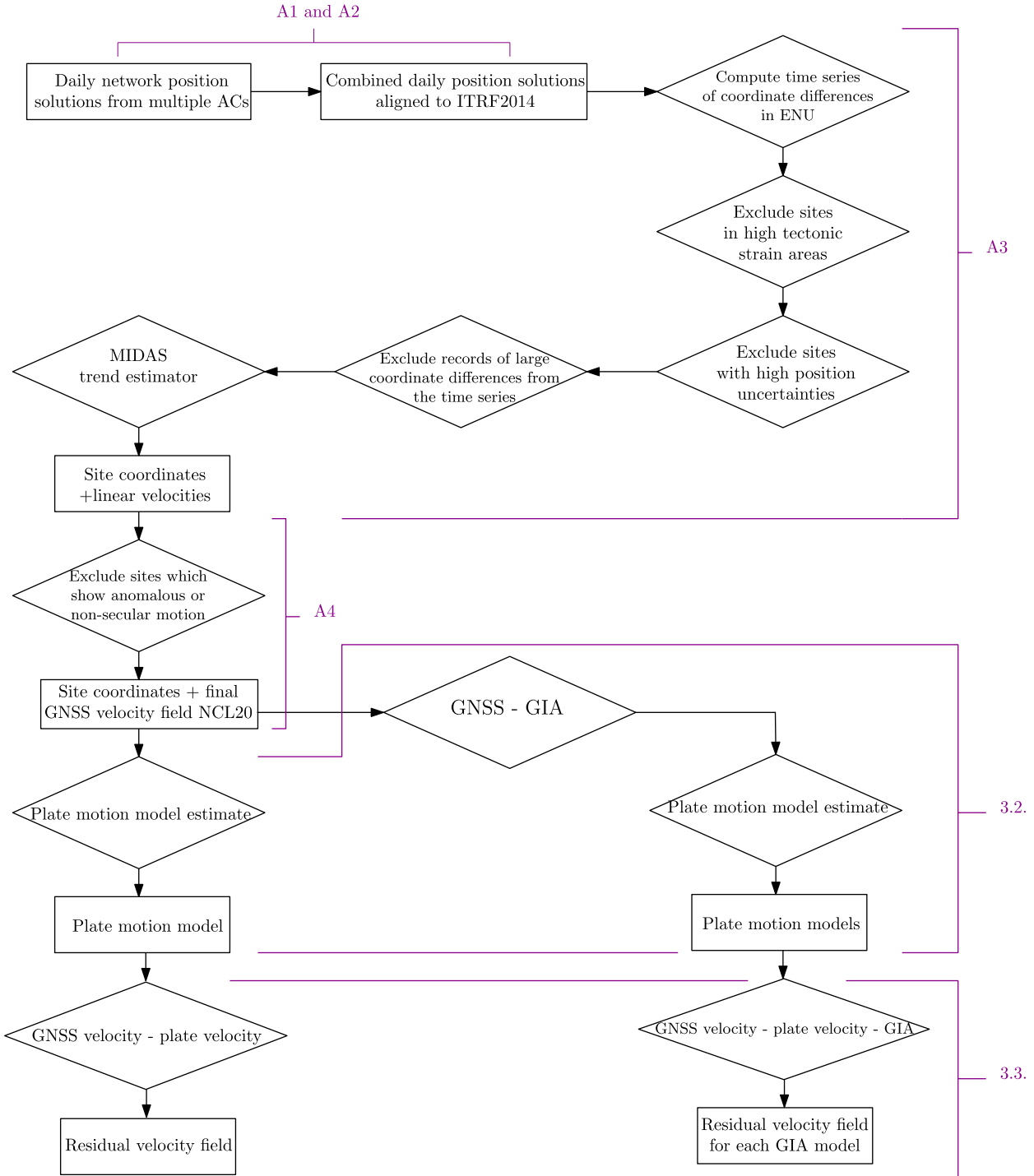


Figure 1. From GNSS network positions to the residual velocity fields. Numbers denote paper sections dealing with the respective step in the process.

by GIA motion, in which case we followed an approach similar to Booker *et al.* (2014), where GIA velocity predictions for each GIA model j are subtracted from the GNSS velocities prior to PMM estimation, according to:

$$\dot{X}^{\text{obs}} - \dot{X}^{\text{GIA},j} = \dot{X}^{\text{corr},j} = \Omega^j \times X + \beta^j + v'. \quad (6)$$

Note that the 1D GIA model predictions are expressed in the centre of mass of the solid Earth (CE), $\dot{X}^{\text{GIA}} \equiv \dot{X}^{\text{GIA[CE]}}$ (omitting the GIA model index j for clarity), while the 3D GIA model predictions

are expressed in a reference frame that assumes no centre of mass motion (CFEM), $\dot{X}^{\text{GIA}} \equiv \dot{X}^{\text{GIA[CFEM]}}$. The GNSS velocities are expressed in the centre of mass of the whole Earth system (CM), $\dot{X}^{\text{obs}} \equiv \dot{X}^{\text{obs[CM]}}$. In the following we let CG represent the GIA model frame which is either CE (for 1D GIA models) or CFEM (for 3D GIA models), and write $\dot{X}^{\text{GIA}} \equiv \dot{X}_i^{\text{GIA[CG]}}$. Thus, site velocities corrected for GIA can be written as

$$\dot{X}^{\text{corr[CM]}} = \dot{X}^{\text{obs[CM]}} - \dot{X}^{\text{GIA[CG]}} - v_{\text{CG-CM}}, \quad (7)$$

where $v_{\text{CG-CM}}$ is the velocity of CG with respect to CM. Considering eqs (6) and (7), we may write:

$$\dot{X}^{\text{obs[CM]}} - \dot{X}^{\text{GIA[CG]}} = \Omega \times X + \beta + v_{\text{CG-CM}} + v' \quad (8)$$

Since $v_{\text{CG-CM}}$ is functionally inseparable from β , we form $\beta' = \beta + v_{\text{CG-CM}}$ and finally obtain:

$$\dot{X}^{\text{corr[CM]}} = \Omega \times X + \beta' + v' \quad (9)$$

for each GIA model j (index omitted). The resulting parameter vector in the least-squares estimate consists of Euler vectors Ω_p for each plate p , and the global velocity vector β' .

The uncertainties of the PMM were propagated from the uncertainties of the input GNSS velocities (variances for each Cartesian component and covariances between the components) through the least-squares adjustment. The Euler pole of each plate (pole longitude Λ_p and latitude Φ_p) and its rotation rate ω_p were computed from the Euler vector Ω_p using the inverse form of eq. (2):

$$\omega_p = \sqrt{\omega_x^2 + \omega_y^2 + \omega_z^2} \quad (10)$$

$$\Lambda_p = \arcsin \omega_z \quad (11)$$

$$\Phi_p = \arctan \frac{\omega_x}{\omega_y}. \quad (12)$$

The uncertainties of Λ_p , Φ_p and ω_p were obtained through error propagation from the uncertainties of the Euler vector.

3.2.2 Geocentre motion

The motion of CG (reference frame origin of a specific GIA model) with respect to CM, together with the geocentre origin rate bias, constitute the global term β' which is obtained in the PMM estimate for each GIA model according to eq. (9). Each GIA model is expressed in a reference frame with an origin in its own realization of CE (1D GIA models) or its own realization of CFEM (3D GIA models) and it is therefore expected that β' will vary depending on the GIA model (*cf. section 4.1*).

Schumacher *et al.* (2018) and King *et al.* (2012b) estimate the origin translations between their GPS data sets and GIA models, and use them to correct vertical GIA velocities following the approach of King *et al.* (2012b). These studies only considered vertical GNSS and GIA velocities. In our study, where horizontal velocities are also taken into consideration, $v_{\text{CG-CM}}$ and the origin rate bias are estimated together for each PMM estimate and used to correct the vertical and horizontal observed velocities when computing the residual velocity fields. It is inconsequential that the term β' is estimated as a single value since the geocentre origin rate bias and $v_{\text{CG-CM}}$ are not needed separately; as a sum, the term β' is relevant for accurate computation of residual velocities. Taking into consideration the differences between reference frame origins of the model and data velocities and taking into consideration the rate of the centre around which the plates rotate, the residuals are ultimately expressed in the desired reference frame of the GNSS velocities.

3.2.3 Outliers

The plate motion models are estimated from all three coordinate components and were first estimated for each plate separately, iteratively excluding outliers. First, a global Chi-square test with ‘standard’ 95 per cent probability is performed on the system of equations of a plate, and if the test fails, we search for outliers with multiple Student’s t -test (Koch 1999). If an outlier is present among

observations, least-squares distributes the error broadly over all the residuals, making the outlier difficult to detect, in addition to the fact that the assumption that the observations follow a Gaussian distribution becomes invalid. Thus, an outlier ∇_i is estimated sequentially for each observation i , that is each velocity component of all sites, with the advantage that the introduction of the outlier will not affect the estimated parameters. A statistical outlier test is obtained when the null hypothesis $H_0: \nabla_i = 0$ is tested against the alternative hypothesis $H_1: \nabla_i \neq 0$. Using the estimated standard deviation of the outlier σ_{∇_i} , the t statistic is given by

$$t = \frac{\nabla_i}{\sigma_{\nabla_i}} \sim t_{n-e-1}, \quad (13)$$

with n being the number of observations and e the number of unknown parameters. H_0 is rejected if $|t| > t_{n-e-1, 1-\alpha/2}$, where α is the significance level for each individual test. In multiple testing, the chance of making a Type I error increases (i.e. the false rejection of H_0), which is here compensated by setting $\alpha = 1 - (1 - \alpha_{\text{tot}})^{1/(n-e)}$, where $\alpha_{\text{tot}} = 0.05$ is the desired overall significance level (Šidák 1967; Teunissen 2017). If an individual measurement record, that is velocity component, is rejected, all three velocity components of the site are rejected before the next iteration of the PMM estimation. Fig. S1 shows the sites that were rejected when seeking to determine the PMM for the GNSS-only velocity field (no GIA model correction). After the removal of outliers for each plate, a global PMM is estimated for all plates together without using any of the rejected sites. Note that these sites have not been excluded from the surface velocity field altogether (they are still considered when computing residuals, see Section 3.3.1); they are only excluded in the PMM estimation associated with a specific GIA model.

When estimating a PMM that accounts for GIA, the only difference to the GNSS-only case is that the predicted GIA velocities are subtracted from the GNSS velocities before estimating the PMM. We denote these PMMs 1D GIA PMMs or 3D GIA PMMs, depending on the type of GIA model subtracted from the GNSS velocities.

We used the tectonic plate boundaries from Bird (2003) to assign a plate to each site (*cf. Fig. A3*). PMMs were only estimated for plates that contain three or more GNSS sites in NCL20: the African, Antarctic, Somalian, Indian, Australian, Eurasian, North American, South American, Nazca, Pacific, Arabian, Sunda, Caribbean, Amurian, Mariana, Yangtze and Panama plates. Given that some sites are excluded in the outlier search process, it is possible that some plates will not have the required minimum three sites after outlier rejection and their PMMs will no longer be estimable. When the outlier search is applied to GIA-corrected input velocities the rejected sites and estimable PMMs may differ between GIA models. Specifically, the Amurian, Mariana and Nazca plates are not estimable in some cases.

Fig. 2 shows the frequency at which each site was rejected while estimating PMMs using the full suite of 1D (top) and 3D (bottom) GIA models (compare with Fig. A4 for the full GNSS site network). The model for estimating PMMs is applied in three geocentric Cartesian dimensions (eq. 9) because it seeks to determine global plate motion and the global vector β' . Therefore a PMM estimation can be affected by vertical outliers as well as horizontal. We note that some sites are excluded with almost all GIA models, whereas some are excluded with a small number of GIA models. There are more excluded sites with 1D GIA models, but there is also a larger number of 1D GIA models. The majority of rejected sites in Figs 2 and A4 are situated in North America and Greenland. However, in North America there is a very high density of sites so

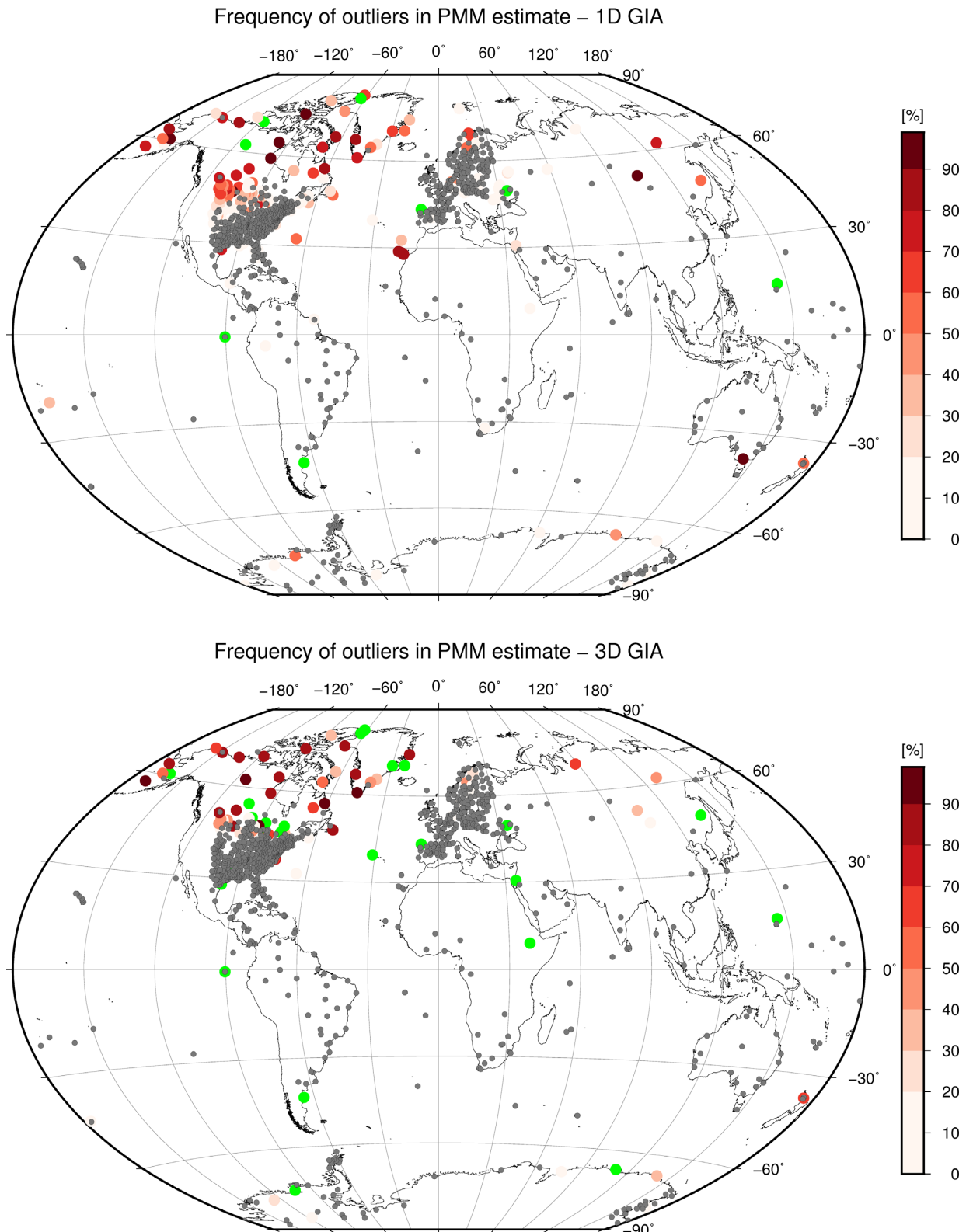


Figure 2. The frequency of outliers to the PMM estimation (Section 3.2.3) for the velocity fields corrected with 1D (top) and 3D (bottom) GIA models. Green denotes the sites that are excluded for all the PMMs. Grey denotes sites that were always included in the final PMM estimate.

neglecting a subset of them for the PMM estimation is not critical. The sites on the west coast of Hudson Bay, where large GIA uplift is expected, and in the northernmost parts of North America, were excluded in the majority of cases. The GNSS-only PMM (Fig. S1)

excluded all these sites from the estimation as well as those in Greenland, where the density of sites is sparse, and several sites in the middle of the Scandinavian peninsula. For GIA PMMs, the Greenland sites are excluded in the majority of cases, but not all,

and in Fennoscandia, a few sites are excluded in a small percentage of cases. For 1D GIA PMMs (Fig. 2 - top), a cluster of sites in the United States and southern Canada were additionally excluded, mostly in a small number of cases, with a few sites in western North America excluded in the majority of cases.

3.3 Comparison of GIA-PMM combinations

3.3.1 Residual velocity fields

We investigated how well the combination of a GIA model and the solved-for plate motion model describe the observed velocity field. After detecting and removing outlier sites, we estimated PMMs using GIA-corrected GNSS velocity fields. We defined a residual velocity field as the velocity field which remains after the GIA model and its associated PMM (including β') have been removed from the GNSS velocity field (eq. 1). It is not expected that, after the removal of plate motion, the GIA effect will be identical to the GNSS displacement at every site. However, since plate motion is removed and tectonically active sites and outliers are excluded, it is expected that the model-predicted GIA velocities should be as close as possible to the GNSS observed displacement at the majority of sites.

To estimate the residual horizontal velocity of a site, we removed the horizontal component of GIA and the plate velocity of that site, as well as the term β' . Residual vertical velocities are calculated by just subtracting GIA and β' . The advantage of the approach taken in this paper is that the PMM used here is estimated taking GIA into account, instead of using a pre-existing PMM which may be biased by GIA. Additionally, this approach of computing residuals includes the term β' which represents variations in frame origins of the GIA models, GNSS network and the centre around which the tectonic plates rotate, thus further improving the residuals.

The plate velocity \dot{X}_i^{pmj} of site i with coordinates X_i is calculated using an equivalent of eq. (3), where the Euler vector of plate p is estimated after correcting the GNSS velocities with GIA model j . We converted \dot{X}_i^{pmj} from the Cartesian XYZ coordinate system to the topocentric ENU coordinate system where \dot{E}_i^{pmj} and \dot{N}_i^{pmj} are easting and northing components of the plate velocity of the site.

Following eq. (9), the residual horizontal velocity of the site is:

$$\dot{E}_i^{\text{res}j} = \dot{E}_i^{\text{GNSS}} - \dot{E}_i^{pmj} - \dot{E}_i^{\text{GIA}j} - \beta'_E \quad (14a)$$

$$\dot{N}_i^{\text{res}j} = \dot{N}_i^{\text{GNSS}} - \dot{N}_i^{pmj} - \dot{N}_i^{\text{GIA}j} - \beta'_N, \quad (14b)$$

where $\dot{E}_i^{\text{GNSS}j}$ and $\dot{N}_i^{\text{GNSS}j}$ are the estimated GNSS velocities in East and North component, respectively, $\dot{E}_i^{\text{GIA}j}$ and $\dot{N}_i^{\text{GIA}j}$ are the predicted GIA velocities in the East and North components and β'_E and β'_N are the local topocentric components of geocentre motion β' from eq. (9). The vertical residual velocity associated with GIA model j is simply computed by removing the Up component of the predicted GIA velocity field and the Up component of β' from the GNSS velocity at the specific site:

$$\dot{U}_i^{\text{res}j} = \dot{U}_i^{\text{GNSS}} - \dot{U}_i^{\text{GIA}j} - \beta'_U. \quad (15)$$

Antarctica is, unlike our other two regions of interest, still largely covered with ice sheets at present. Thus, the residual velocity field in this region was additionally corrected for the elastic response to present-day ice mass changes (e.g. Bevis *et al.* 2009; Thomas *et al.* 2011; Whitehouse 2018; Schumacher *et al.* 2018). Elastic corrections were provided by Achraf Koulali (personal communication,

2020) and applied to both the horizontal and vertical velocity components. They were computed closely following the approach of Shepherd *et al.* (2019). The approach exploits ice sheet surface elevation changes, as determined from multimesh satellite altimetry, with ice mass fluctuations isolated using a firn densification model and the surface mass balance anomaly output from a regional climate model. The elastic response to present-day ice mass trends was computed using the Regional ElAstic Rebound (REAR) calculator (Melini *et al.* 2014). Our calculations do not include the non-tidal ocean load necessary to conserve mass, but this effect is small especially inland of the grounding line. Calculated elastic rates at the Antarctic GNSS sites are shown in Fig. S11. The uncertainties of the elastic correction were derived via Monte Carlo simulation and propagated together with the GNSS uncertainty to obtain the final uncertainty of the residuals in Antarctica.

3.3.2 Median absolute deviations (MADs)

To assess how well each GIA model and its associated PMM explain the observed velocity field, we compared the residual velocity fields obtained after the GIA model predictions and the corresponding PMMs have been subtracted from the GNSS velocity field. We used Median Absolute Deviations (MADs) as a measure of goodness of fit of the models with respect to the observed GNSS velocities. We consider models with smaller MADs to be better models. MAD is computed as follows:

$$MAD = \text{median}|\dot{X}_{\text{obs}} - \dot{X}_{\text{modelled}}|, \quad (16)$$

where $\dot{X}_{\text{obs}} - \dot{X}_{\text{modelled}}$ are the residuals $\dot{E}_i^{\text{res}j}, \dot{N}_i^{\text{res}j}, \dot{U}_i^{\text{res}j}$ from eqs (14) to (15), associated with GIA model j , where i is the site number which ranges over all the sites in a selected region. We computed the MAD for the horizontal component,

$$MAD_{\text{hor}}^j = \text{median}\left(\sqrt{(\dot{E}_i^{\text{res}j})^2 + (\dot{N}_i^{\text{res}j})^2}\right), \quad (17)$$

and for the vertical component:

$$MAD_{\text{up}}^j = \text{median}|\dot{U}_i^{\text{res}j}|. \quad (18)$$

To assess whether applying a correction for GIA improves the goodness of fit, MADs for the GNSS velocity field without any GIA correction (i.e. a GNSS-only PMM) were also computed, which we denote as the null-GIA case. The MADs were computed globally and for our selected regions of interest, namely Europe, North America and Antarctica. Note that for Europe, the tectonic plate to which the site velocities are fitted is Eurasian, whereas the goodness of fit of the models is chosen based on the fit of velocities in northern Europe as this is the only area on the Eurasian Plate where the choice of GIA model can significantly affect the plate model.

Computation of global MADs is potentially biased by the significantly higher density of GNSS sites in the United States network, on the North American Plate. To mitigate this, global MADs were determined by computing a separate MAD for each plate and weighting by plate area, according to

$$MAD_{\text{weighted}}^j = \frac{\sum_{p=1}^n A_p \times MAD_p^j}{\sum_{p=1}^n A_p}, \quad (19)$$

where MAD_p^j and A_p are the MAD and area of each estimated plate p , and MAD_{weighted}^j is the global plate-weighted MAD.

Table 1. Minimum and maximum MAD values for all GIA models in each category.

	Horizontal 1D	Horizontal 3D	Median absolute deviation [mm yr ⁻¹]	Vertical 1D	Vertical 3D	Vertical null-GIA
	Horizontal null-GIA	Vertical 1D	Vertical 3D	Vertical null-GIA		
Europe	0.40–0.78	0.40–0.49	0.44	0.55–1.31	0.71–1.25	1.29
North America	0.60–1.66	0.62–0.78	0.68	0.75–2.19	0.87–1.26	1.07
Antarctica	0.86–1.86	1.01–1.28	1.07	1.84–4.09	1.22–2.61	1.31
Global plate weighted	0.66–1.01	0.58–0.64	0.60	0.98–1.64	0.88–1.14	1.02
Global no weighting	0.57–1.21	0.56–0.68	0.60	0.78–1.76	0.91–1.22	1.12

We computed MADs for all GIA models in categories which are combinations of the following:

- (i) Region — global, Europe, North America or Antarctica
- (ii) GIA model Earth structure — 1D or 3D (or null-GIA)
- (iii) Horizontal or vertical component

The MAD values for each region and velocity component were compared, and the models with the smaller MAD are considered better models. As mentioned, it is not expected that the sum of the GIA model predictions and the plate motion model will be equivalent to the GNSS displacement at every site. The residual motion at the majority of sites should be close to zero, but large residuals can only unequivocally indicate that the observed motion is not in agreement with the modelled GIA prediction. The resulting misfits can be due to the fact that the GIA model predicts too much or too little GIA motion compared to the true values, which are unknown. Misfits may also be due to processes not related to GIA that cause uplift, subsidence or horizontal motion, such as local tectonics or present-day ice mass changes. Antarctica and Greenland are examples of areas affected by GIA and the solid Earth response to present-day ice mass changes. In Antarctica, which is one of the areas of interest in this study, the effect of present-day ice mass change is accounted for in eqs (14) and (15) by subtracting an additional elastic deformation term. We do not focus on Greenland in this study due to the lack of sufficient high-quality GNSS data. Not correcting the Greenland sites for the effect of present-day ice mass change will have an insignificant impact on the global MAD because the North American Plate MAD is dominated by the very high number of sites outside of Greenland.

The GIA model with the smallest MAD in each category is selected as the best GIA model. Next, groups of ‘near-best’ models in each category were formed using an MAD criterion, that is by considering all models with MADs better than the null-GIA case and within a threshold of 0.1 mm yr⁻¹ and 0.2 mm yr⁻¹ of the best model for the horizontal and the vertical component, respectively. These thresholds were chosen based on the spread of MADs as well as the GNSS uncertainties for each velocity component. The GNSS velocity uncertainties are mostly up to 0.5 mm yr⁻¹ in the horizontal component and 1 mm yr⁻¹ in the vertical component (*cf.* Section 4), with 0.1 mm yr⁻¹ and 0.2 mm yr⁻¹ being 20 per cent of these values. The MADs vary between 0.4 mm yr⁻¹ and 1.9 mm yr⁻¹ for the horizontal component and 0.5–4.1 mm yr⁻¹ for the vertical component (*cf.* Table 1).

The groups of near-best models represent the models that are nearly as good as the best model according to the MAD criterion above, that is any of them could have been the best model if a different observation data set were used, considering the number of sites per plate and their uncertainties. Tables B2–B5 list the models in the groups of near-best models. Table 2 shows the number of GIA models assigned to each group of near-best models. The groups

marked with \emptyset are the ones where even the best fitting GIA model was no better than the null-GIA case.

The MADs are used as a measure of GIA model goodness of fit. They represent the residual velocity field which remains after removing GIA and plate motion models from the NCL20 GNSS velocities (see eq. 16). The ‘best’ GIA model and ‘near-best’ GIA models are chosen according to the MADs (Section 3.3.2). The GIA models are ranked separately for the global case and for each region of interest (Europe, North America and Antarctica). The best and near-best PMMs are also chosen according to the MADs, that is the ranking of the PMM is based on the ranking of the GIA model that was used to create that PMM. The best GIA models in the horizontal component are not necessarily the best GIA models in the vertical component, and vice versa. Since the horizontal component is the one that is more likely to contaminate the PMM estimate, given that rigid plate motion is horizontal only, we define the best PMMs to be the ones that are estimated with the best GIA models in the horizontal component.

4 RESULTS

We denote our GNSS velocity field NCL20 (Fig. 1). It contains 965 sites, where for about 70 per cent of the sites the horizontal velocity uncertainties are within 0.5 mm yr⁻¹, and vertical velocity uncertainties within 1 mm yr⁻¹ (*cf.* Fig. 3). The GNSS site names, locations, velocities and velocity uncertainties are listed in Vardić *et al.* (2021).

4.1 Plate motion models

The PMMs were estimated according to eq. (4) and eq. (9) which resulted in 117 global PMMs estimated with velocity fields corrected using each of the GIA models (81 1D GIA models and 36 3D GIA models) and a global PMM estimated using the GNSS velocity field without any GIA corrections.

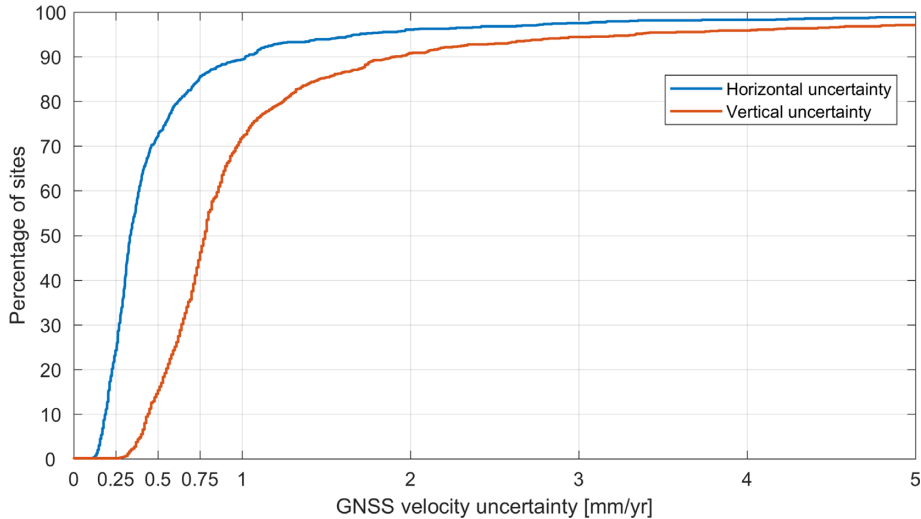
The Euler pole locations estimated using the uncorrected GNSS velocity field (GNSS-only PMM) are shown on a global map in Fig. 4.

The CG-CM (i.e. CE-CM or CFEM-CM) translations and the origin bias for each PMM (named β for GNSS-only PMM and β' for GIA PMMs, *cf.* Section 3.2.1) are listed in Table S1. The uncertainty of β for the GNSS-only PMM is $\sigma_{\beta_X} = 0.002 \text{ mm yr}^{-1}$, $\sigma_{\beta_Y} = 0.002 \text{ mm yr}^{-1}$ and $\sigma_{\beta_Z} = 0.001 \text{ mm yr}^{-1}$.

For each region of interest we analyse the GNSS-only PMM, ITRF2014 PMM and GIA PMMs, particularly the best and near-best (*cf.* Section 3.3.2) GIA PMMs.

Table 2. Number of GIA models in the groups of near-best GIA models for each category.

	Global	Europe	North America	Antarctica	Total no. models
Horizontal 1D	∅	6	7	6	81
Horizontal 3D	13	9	30	6	36
Vertical 1D	3	25	6	∅	81
Vertical 3D	18	18	16	4	36

**Figure 3.** Empirical cumulative distribution functions of the site velocity uncertainties in the horizontal (easting and northing velocity standard deviation combined into horizontal magnitude uncertainty) and vertical (Up velocity standard deviation) components for the final GNSS velocity field.

4.1.1 All plates

As mentioned above, the globally best-fitting GIA model is chosen according to its MAD, which can be calculated in two ways, by weighting the MADs by plate area or without any weighting. The best PMM globally is then chosen to be the PMM associated with the best fitting GIA model. Globally, the best PMM when weighting is applied is the PMM estimated using GIA model 6G_SL_wet_10mm ($\text{MAD} = 0.58 \text{ mm yr}^{-1}$). The best PMM when no weighting is applied is the PMM estimated using GIA model 6G_S_dry_4mm ($\text{MAD} = 0.56 \text{ mm yr}^{-1}$). We consider the weighted case to be more realistic, since weighting the global MAD by plate area reduces the biasing effect of small areas with a large density of sites. Therefore, the PMM derived using the 6G_SL_wet_10mm GIA model is the one, among our ensemble of PMMs, that is to be used when investigating global plate motion (see Table 3).

Fig. 5 shows individual Euler pole locations for all the plates estimated within this study (see Fig. 4 for locations on a global map). The figures show Euler pole locations for all 1D GIA PMMs, 3D GIA PMMs and the GNSS-only PMM as well as emphasizing the location of the two globally best GIA-corrected PMMs (plate-weighted and non plate-weighted) and their error ellipses (95 per cent confidence). For comparison, we include Euler pole locations for a geological PMM [MORVEL56 PMM; Argus *et al.* (2011)] and a previously published space-geodetic PMM [ITRF2014 PMM; Altamimi *et al.* (2017)]. For the majority of plates, the MORVEL56 PMM shows only a loose agreement with Euler pole locations from the ITRF2014 PMM and the PMMs estimated here.

Euler poles of the globally best models with and without plate-weighting are not located in the same place. The globally (weighted) best PMM is created using a 3D GIA model. The ITRF2014 PMM

Euler poles are for most plates closer to the 3D GIA PMMs or similarly distant from the 1D and 3D GIA PMMs, but for the Australian and South American plates they are closer to the 1D GIA PMMs. The distribution of Euler pole locations for the North American, Eurasian and Antarctic plates is described in detail in the following sections. Euler pole locations for other plates are typically spread over 300–400 km, except for the South American Plate, where they are spread over ~ 530 km east–west and up to ~ 800 km north–south.

4.1.2 Eurasian plate

Fig. 6(a) shows Euler pole locations and rotation rates for the Eurasian Plate estimated using the GNSS-only velocity field or a velocity field corrected using the near-best (Eurasian-specific) 1D and 3D GIA models. The Euler poles for the near-best 1D GIA PMMs are grouped closely together over ~ 50 km east–west and ~ 130 km north–south while the near-best 3D GIA PMM Euler poles are grouped in two areas and span over ~ 250 km east–west and ~ 140 km north–south.

The Euler pole locations in Fig. 6(a) show that the 1D GIA PMM pole locations are closer together (some within their 99 per cent position probabilities) than the 3D GIA PMM Euler poles. The best 3D GIA PMM Euler pole is significantly closer to the ITRF2014 PMM and GNSS-only PMM than the best 1D GIA PMM. Since the ITRF2014 PMM was created empirically by excluding sites in GIA affected areas, this suggests that the 3D GIA models could be better at correcting for plate-like GIA motion. The two near-best groups show a similar spread of rotation rates, with values typically smaller than for the ITRF2014 PMM, especially for the 3D GIA PMMs (Fig. 6a). The uncertainty of the Eurasian rotation rates for

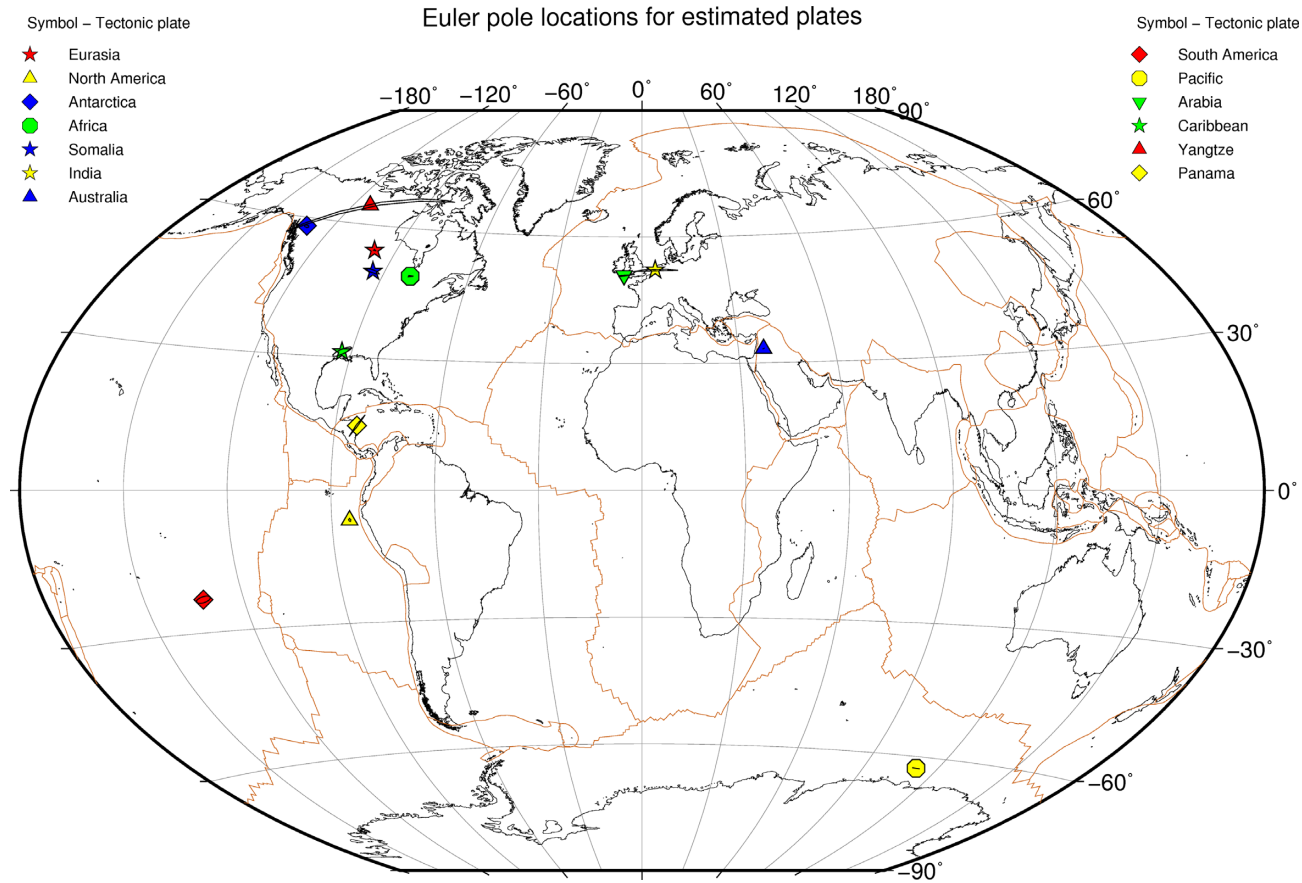


Figure 4. Euler pole locations for all tectonic plates estimated with our GNSS velocity field. The error ellipses (in black) are 95 per cent confidence limits (close-up view in Fig. 5). The light brown lines show the tectonic plate boundaries for all tectonic plates from Bird (2003).

the GNSS-only PMM and near-best GIA PMMs is $0.0005^\circ \text{ Myr}^{-1}$. The difference in rotation rate between our estimated PMMs and the ITRF2014 PMM is therefore significant.

To investigate whether the differences in Euler pole locations and rotation rates have a significant effect on modelled plate velocities, we estimated plate velocities using a suite of different PMMs. Plate velocities in Europe point in a NE direction and are on average $\sim 15 \text{ mm yr}^{-1}$ (Figs S5 and S6). We find that differences between plate velocities estimated using the near-best 1D GIA PMMs are below 0.5 mm yr^{-1} (see Fig. S5). The respective differences for the near-best 3D GIA PMMs are up to 1 mm yr^{-1} . Differences between the best 1D GIA PMM plate velocities and the ITRF2014 PMM and GNSS-only PMM plate velocities are up to 2 mm yr^{-1} in Europe (see Fig. S6). The respective differences for the best 3D GIA PMM are mostly up to 1 mm yr^{-1} . This indicates that for the analysed PMMs in Europe, differences in estimated Euler pole location have a greater impact on modelled plate velocities than differences in estimated rotation rate.

Consequently, although the ITRF2014 PMM and GNSS-only PMM rotation rates are closer to that of the best 1D GIA PMM (Fig. 6a), their Euler pole locations and modelled plate velocities are more similar to those of the best 3D GIA PMM (Fig. S6). This shows that the 3D GIA PMMs are more similar to the ITRF2014 PMM than the 1D GIA PMMs, suggesting that the 3D GIA PMMs are better at correcting for horizontal GIA in Europe.

4.1.3 North American plate

Figs 6(b) and (c) show Euler pole locations for the North American tectonic Plate for the near-best 1D and 3D GIA PMMs, and the GNSS-only PMM, as well as the ITRF2014 PMM. The uncertainty of the rotation rates is $0.0005^\circ \text{ Myr}^{-1}$, similar to the Eurasian Plate. Within the near-best 1D GIA PMMs, rotation rates vary mostly up to $0.001^\circ \text{ Myr}^{-1}$, within the near-best 3D GIA PMMs they vary more, up to $0.02^\circ \text{ Myr}^{-1}$, but the majority of the Euler poles are closer to each other. The near-best 1D GIA PMMs have rotation rates closer to the ITRF2014 PMM than the 3D GIA PMMs do. However, the Euler poles of the 1D GIA PMMs are located further from the ITRF2014 PMM Euler pole, similar to our findings in Eurasia. Since the Euler pole for the North American Plate is located close to the plate itself (*cf.* Fig. 4), a change in pole location has a significant impact on the velocity of points on the plate.

We compute plate velocities using the GNSS-only and GIA PMMs and the ITRF2014 PMM, as well as differences of plate velocities between models, as presented above for Europe (Figs S7 and S8). The North American tectonic Plate is rotating anti-clockwise with plate velocities of $\sim 19 \text{ mm yr}^{-1}$ on average. Differences between plate velocities obtained using the near-best 1D GIA PMMs are mostly up to $\sim 0.5 \text{ mm yr}^{-1}$ with some differences up to 1 mm yr^{-1} (Fig. S7). Plate velocity differences for the near-best 3D GIA PMMs vary from below 0.5 mm yr^{-1} up to 1.9 mm yr^{-1} . The larger velocities pointing south are evaluated with the three models

Table 3. Plate motion model estimated after correcting the GNSS velocity field with the globally best-fitting GIA model, when applying weighting by plate. GIA corrections are obtained from the model 6G_SL_wet.10mm. NS stands for the number of sites on each plate in this PMM, and NS-ITRF14 stands for the number of sites on each plate in the ITRF2014 PMM. \emptyset denotes plates which were not estimated in the ITRF2014 PMM.

Plate	ω_x	ω_y [$^{\circ}$ Myr $^{-1}$]	ω_z	Longitude [$^{\circ}$]	Latitude [$^{\circ}$]	ω [$^{\circ}$ Myr $^{-1}$]	NS	NS-ITRF14
African (Nubia)	0.0286	-0.1678	0.1944	-80.33	48.79	0.2584	23	24
\pm	0.0009	0.0006	0.0006	0.29	0.11	0.0007		
Antarctic	-0.0741	-0.0921	0.1928	-128.83	58.49	0.2262	55	7
\pm	0.0006	0.0006	0.0012	0.25	0.18	0.0011		
Somalian	-0.0139	-0.1919	0.2232	-94.15	49.24	0.2947	7	3
\pm	0.0026	0.0025	0.0017	0.72	0.26	0.0029		
Indian	0.3178	0.0268	0.4134	4.82	52.35	0.5221	7	3
\pm	0.0026	0.0115	0.0036	2.02	0.14	0.0049		
Australian	0.4203	0.3217	0.3457	37.43	33.15	0.6322	26	36
\pm	0.0008	0.0007	0.0007	0.10	0.05	0.0007		
Eurasian	-0.0228	-0.1445	0.2018	-98.97	54.06	0.2492	229	97
\pm	0.0004	0.0005	0.0005	0.17	0.11	0.0005		
North American	0.0120	-0.1895	-0.0177	-86.39	-5.32	0.1907	461	72
\pm	0.0005	0.0005	0.0004	0.14	0.14	0.0005		
South American	-0.0744	-0.0826	-0.0428	-132.02	-21.08	0.1191	35	30
\pm	0.0012	0.0013	0.0007	0.86	0.32	0.0007		
Pacific	-0.1132	0.2898	-0.5955	111.34	-62.42	0.6719	21	18
\pm	0.0008	0.0005	0.0006	0.16	0.04	0.0006		
Arabian	0.3147	-0.0353	0.3940	-6.41	51.21	0.5054	6	5
\pm	0.0043	0.0049	0.0030	0.97	0.15	0.0046		
Caribbean	-0.0176	-0.2593	0.1601	-93.88	31.64	0.3053	10	\emptyset
\pm	0.0037	0.0091	0.0032	0.95	0.50	0.0091		
Yangtze	-0.0578	-0.1272	0.2933	-114.45	64.53	0.3249	3	\emptyset
\pm	0.0084	0.0161	0.0108	5.84	2.60	0.0050		
Panama	0.1597	-1.4765	0.3935	-83.83	14.84	1.5363	5	\emptyset
\pm	0.0516	0.2796	0.0454	0.82	1.08	0.2856		

whose Euler poles are located far from the main cluster of near-best 3D GIA PMMs (see Fig. 6c). These PMMs were created using GIA models that combine each of the three ice models with the same 3D Earth model (SL seismic velocity model (Schaeffer & Lebedev 2013), dry rheology and 10 mm grain size). Differences between the plate velocities derived using the best 1D GIA PMM and the GNSS-only PMM are on average 0.7 mm yr^{-1} , whereas differences between the best 1D GIA PMM and the ITRF2014 PMM are $1\text{--}2 \text{ mm yr}^{-1}$, with the greatest discrepancies found in the eastern part of the continent (Fig. S8). Differences between the best 3D GIA PMM and the GNSS-only PMM are 0.4 mm yr^{-1} on average, whereas for the best 3D GIA PMM and the ITRF2014 PMM they range from 0.5 mm yr^{-1} in the west to over 1.5 mm yr^{-1} in the east. The Euler pole for the best 3D GIA PMM is 117 km closer to the ITRF2014 Euler pole than the best 1D GIA PMM Euler pole (Figs 6c and d), and its velocities are more similar to the ITRF2014 PMM (Fig. S8), strongly suggesting that the 3D GIA model may be better at correcting horizontal GIA motion. Comparing these plate velocity differences with Euler pole locations, we come to the same conclusion as for Eurasia, that the influence of Euler pole location on plate velocities is greater than the influence of Euler pole rotation rate.

4.1.4 Antarctic plate

Figs 6(d) and (e) show Euler pole locations and rotation rates for the Antarctic tectonic Plate for the near-best 1D GIA PMMs, near-best 3D GIA PMMs, GNSS-only PMM and ITRF2014 PMM. The

best 3D GIA PMM Euler pole is closer to the GNSS-only PMM Euler pole than the best 1D GIA PMM (232 km for the 1D and 151 km for the 3D GIA PMM). The near-best 3D GIA PMM Euler poles are spread in the east–west direction, and some are very close in rotation rate and Euler pole location to the GNSS-only PMM. This could be because the GIA corrections for these models are so small that the resulting PMMs are similar to the GNSS-only PMM. The best 1D and 3D GIA PMM Euler poles are 94 km and 45 km from the ITRF2014 PMM Euler pole, respectively. However, both are located within the ITRF2014 PMM Euler pole location uncertainty. The best 1D GIA PMM has a rotation rate more similar to the ITRF2014 PMM rotation rate than that of the best 3D GIA PMM. The rotation rates among most PMMs are similar to each other, when compared with the larger variation of rotation rates observed for the Eurasian and North American plates. However, the uncertainties of the rotation rates for the Antarctic Plate are larger than for the Eurasian and North American plates, $0.001^{\circ} \text{ Myr}^{-1}$ for our PMMs and $0.002^{\circ} \text{ Myr}^{-1}$ for the ITRF2014 PMM.

We computed the modelled plate velocities and their differences as above for Europe and North America (Figs S9 and S10). The Antarctic tectonic Plate is rotating clockwise with plate velocities ranging from $\sim 20 \text{ mm yr}^{-1}$ in the west and central part of the Antarctic continent to $\sim 5 \text{ mm yr}^{-1}$ in the east. The differences between plate velocities evaluated with the near-best 1D and 3D GIA PMMs are both on average 0.4 mm yr^{-1} (Fig. S9), but they point in different directions for the 1D GIA PMMs and mostly in the same direction for the 3D GIA PMMs. Differences between plate

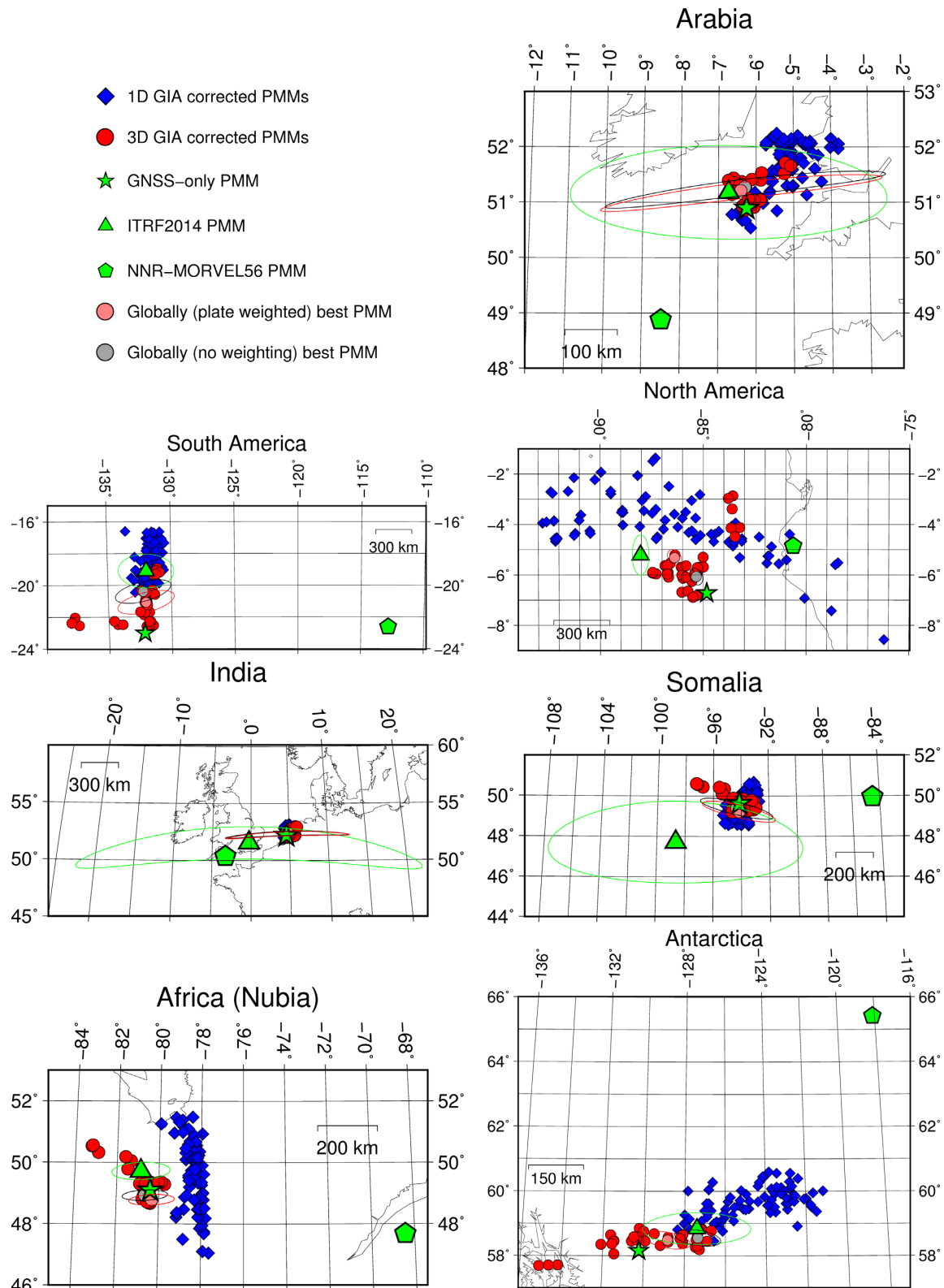


Figure 5. Euler pole locations for all PMMs, for all estimated tectonic plates. The error ellipses are 95 per cent confidence limits: red for the globally best PMMs when weighting by plate area is applied, black without weighting and green ellipse for the ITRF2014 PMM. No error information is available for NNR-MORVEL56. The ITRF2014 and MORVEL56 PMMs do not consider all of the plates shown here (see plates where the triangle or pentagon symbol is missing).

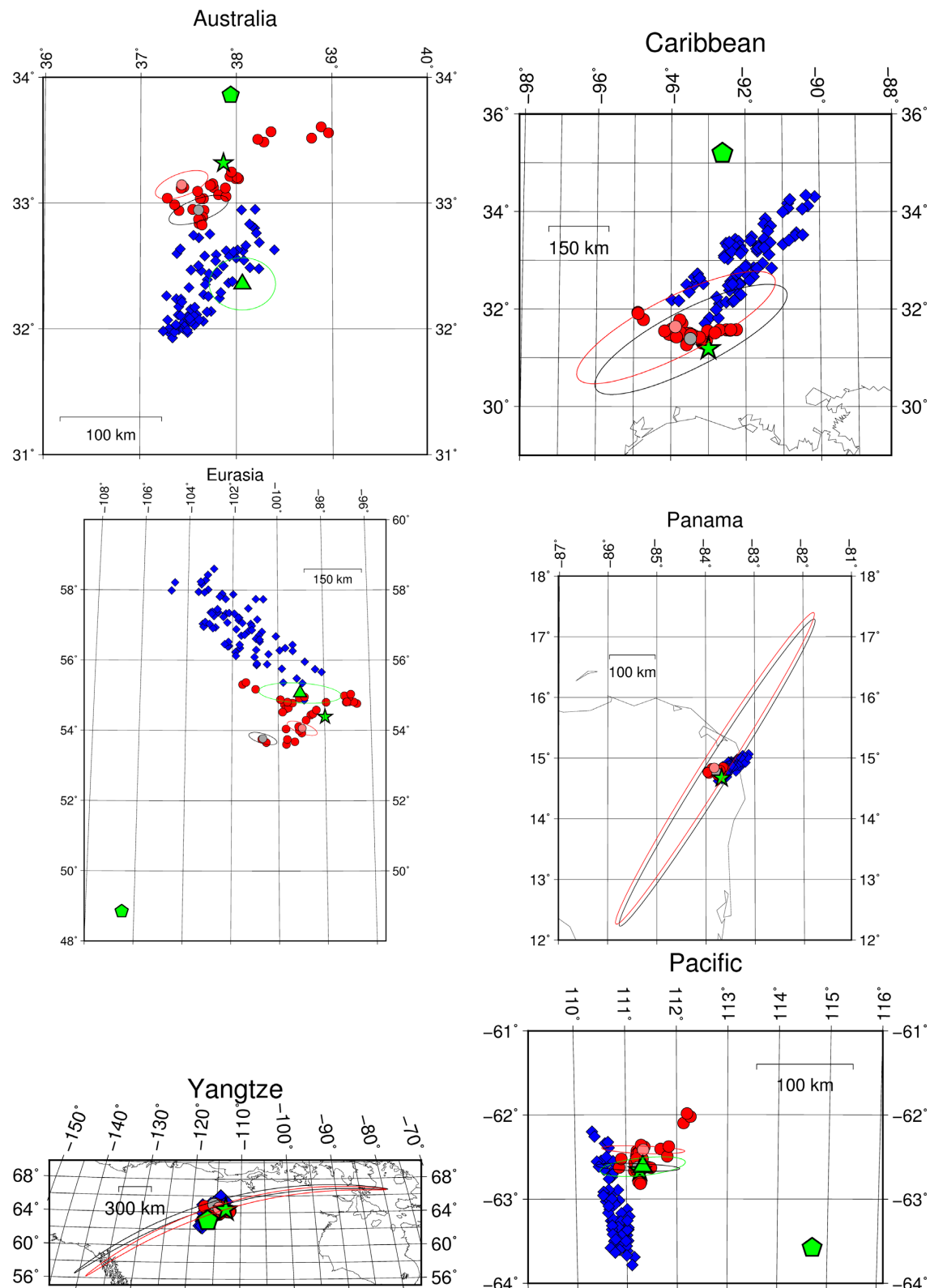


Figure 5. continued.

velocities generated using the GNSS-only PMM and the best 1D GIA PMM are on average 1.2 mm yr^{-1} (Fig. S10). Differences between the best 3D GIA PMM plate velocities and the GNSS-only PMM plate velocities are smaller, on average 0.6 mm yr^{-1} . The latter point in a similar direction to the differences between the 1D GIA

PMM and the ITRF2014 PMM, which are on average 0.4 mm yr^{-1} . Differences in plate velocities estimated using the best 3D GIA PMM and the ITRF2014 PMM are on average 0.6 mm yr^{-1} . They point in a similar direction to the plate velocities estimated using the best 1D/3D GIA PMM, meaning that the velocity vectors differ

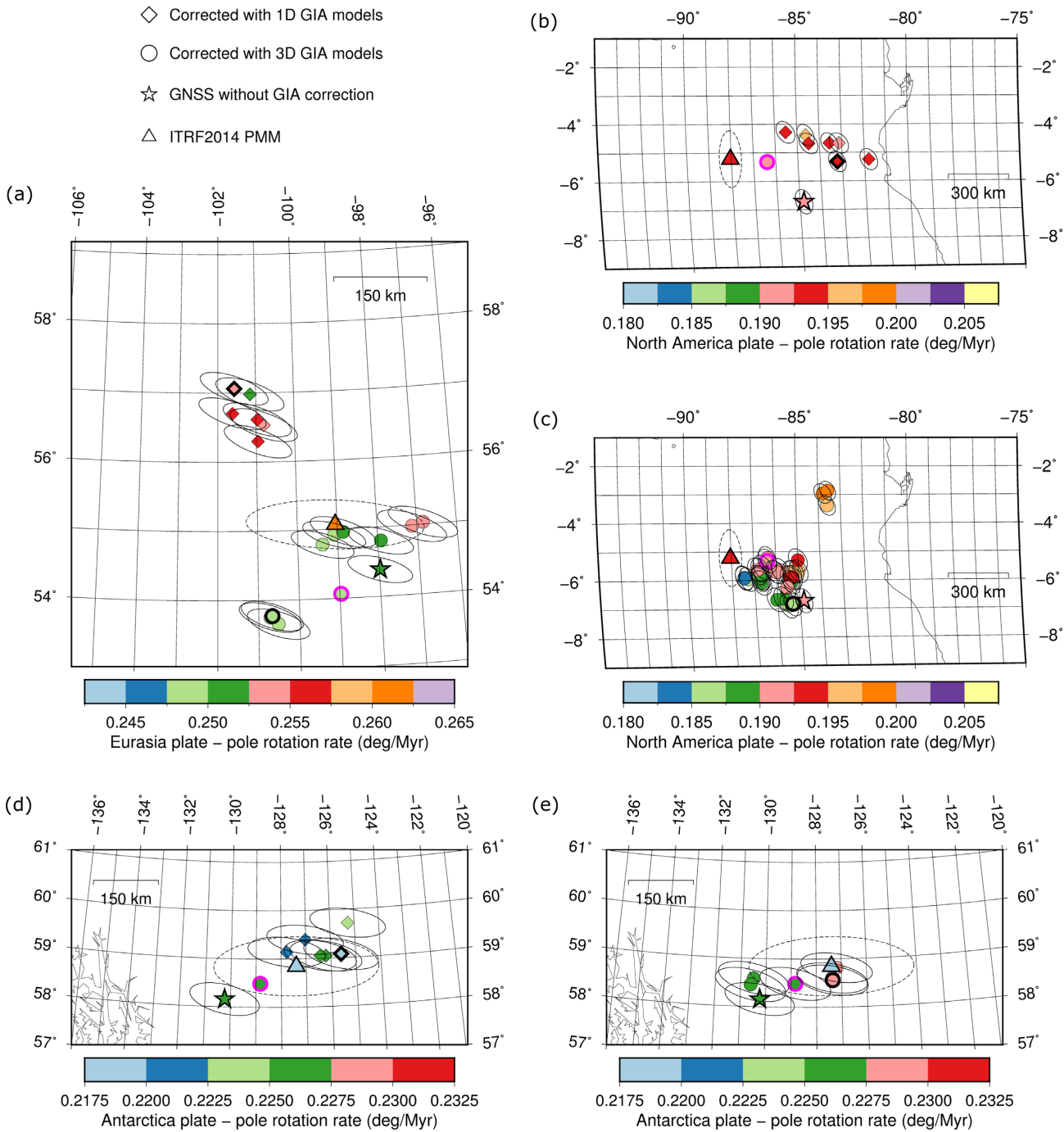


Figure 6. Euler pole locations for the Eurasian, North American and Antarctic tectonic plates: (a) Eurasia near-best 1D and 3D GIA PMMs, (b) North America near-best 1D GIA PMMs, (c) North America near-best 3D GIA PMMs, (d) Antarctica near-best 1D GIA PMMs, (e) Antarctica near-best 3D GIA PMMs. Error ellipses represent 99 per cent probability of the pole location (dashed error ellipse is for ITRF2014 PMM for each respective plate). The uncertainty of the rotation rate is 0.00047 , 0.00046 and 0.001° Myr $^{-1}$ for the Eurasian, North American and Antarctic Plate, respectively. The bold black-rimmed symbol (circle or diamond) represents the best model for each plate among the 1D and 3D GIA PMMs. The magenta-rimmed symbol represents the globally (plate weighted) best model.

mostly in magnitude rather than direction. Similar plate velocity direction and different velocity magnitude indicate similar pole location and different rotation rate. This indeed is the case for the Euler poles of the best 3D GIA PMM and the ITRF2014 PMM in Fig. 6.

In Antarctica, when comparing with the ITRF2014 PMM we must take into consideration the fact that none of the sites were excluded

in the ITRF2014 PMM estimation, but almost the entire plate is affected by GIA. Additionally, our study uses far more observation sites (55 sites compared with 7 sites for the ITRF2014 PMM) and so the uncertainty of our Euler vector for Antarctica is much smaller. The ITRF2014 PMM Euler pole is, as mentioned above, closer to the best 1D GIA PMM in rotation rate, but closer to the best 3D GIA PMM in pole location. The plate velocities estimated with the

ITRF2014 PMM are more similar to the plate velocities from the best 1D GIA PMM. This may suggest that in Antarctica, a change in rotation rate has a greater influence on plate velocities than a change in pole location. However, these differences may also be due to the fact that the Euler poles of the best 1D GIA PMM and 3D GIA PMM are located quite close to each other, ~ 50 km. The Euler pole for the Antarctic plate is located very far from the plate itself (see Fig. 4), so differences in Euler pole location have a relatively minor influence on plate velocities.

4.2 GIA model assessment

We have compared the MAD values of all our GIA models and identified certain features of GIA models which are, in combination with their respective PMMs, most compatible with the GNSS observations. These are summarised in Table 4. Unlike the 3D GIA models, the 1D GIA models show a preference for ice model ICE-6G in all regions (see also Tables B2–B5). Due to the different input parameters of 1D and 3D Earth models, it is not straightforward to compare the preferred rheological properties of 1D and 3D GIA models in each region. For the 1D GIA models, while there is no preference for lithosphere thickness in the vertical component, in the horizontal component, a thicker lithosphere is preferred in all cases besides Antarctica. Note that for the global case (plate weighted), when considering horizontal velocities, none of the 1D GIA models has a smaller MAD value than the null-GIA case (*c.f.* Table 2). This suggests that it is not possible to identify a 1D GIA model that robustly replicates the global GIA signal.

Since, by definition, the group of near-best models is close to the best model in terms of the MAD value for each region, studying the differences in GIA predictions among the near-best models provides insight into GIA model uncertainty for each region. For each group of near-best GIA models, the range of GIA model predictions is computed for each grid point in the region. This tells us where the predictions of credible GIA models differ the most, and reveals the areas that are sensitive to a change in Earth or ice model parameters. For the vertical component, the range is defined to be the difference between the maximum and minimum GIA prediction at each point. For the horizontal component, the range is defined to be the difference between the largest and smallest magnitude of the GIA prediction at each point. In the horizontal component, the maximum and minimum azimuths are also identified (the range of directions of the horizontal velocities). Due to our interest in understanding how GIA may bias plate motion models, we focus below on differences in GIA predictions of horizontal motion.

4.2.1 Europe

Figs 7(a) and (b) show the magnitude and azimuth ranges of horizontal GIA predictions across Europe for the 6 near-best 1D models and the 9 near-best 3D models (see also Fig. S12). The 1D models have the largest magnitude range of $0.8\text{--}1.0 \text{ mm yr}^{-1}$ in the area east of the Lofoten archipelago. This range reduces gradually from NW to SW (Fig. S12a). The range in velocity directions for these models is mostly below $\sim 30^\circ$, with the largest range in directions found to the east of the Gulf of Bothnia. Any differences between the 1D GIA model predictions will be due to differences in Earth properties because all of the near-best horizontal 1D models were created using the same ice model. The 3D models show a smaller range in horizontal magnitude than the 1D models, with a maximum range of 0.75 mm yr^{-1} found in northern Norway. Similarly,

we found that the 3D models show a smaller range of vertical predictions (not shown). However, the 3D models show a larger range in velocity directions than the 1D models. The reason for this could be that the near-best 3D models are based on three different ice models, whereas the near-best 1D models are all based on the same ice model.

We compute the residual horizontal velocity field at GNSS sites across Europe using the best 1D (6G_96p310) and 3D (6G_S_dry_4mm) GIA models for this region, as defined by the MAD values for horizontal velocities (Figs 8a and b). Both models have MADs of 0.40 mm yr^{-1} (Table 1), although all their plate vectors and velocities are different. In both cases the sites with the largest residual horizontal velocities (over 1.5 mm yr^{-1}) are those with the largest GNSS uncertainties. In Fennoscandia, the best 1D GIA model gives residual magnitudes below 0.8 mm yr^{-1} at most sites, with a few sites showing values between 1 mm yr^{-1} and 1.3 mm yr^{-1} . Residual velocities on the west coast of Norway point northwards, but their magnitudes are $\sim 0.5 \text{ mm yr}^{-1}$. This is close to the level of uncertainty of GNSS velocities in this region so these values are hardly significant and should be interpreted with care. Elsewhere, residual velocities of $0.5\text{--}0.6 \text{ mm yr}^{-1}$ are found on the west coast of the Gulf of Bothnia pointing SE, inwards to the Gulf of Bothnia. This may indicate that the best 1D GIA model overpredicts horizontal motion in this area, or that motion is predicted in the wrong direction, perhaps due to inaccuracies in the deglaciation history. The main difference in performance between the best 1D and 3D models in the horizontal component is on the coast of Norway and in the centre of the Scandinavian peninsula, where the 3D model shows larger residuals, all in the NW direction. Further work is needed to determine whether these misfits reflect a bias in the PMM or the fact that the ice model was developed assuming 1D Earth structure.

4.2.2 North America

Figs 7(c) and (d) show the range of horizontal magnitudes and the range of directions of GIA velocity predictions in North America for our near-best models (see also Fig. S12). There are 7 models in the group of near-best 1D models and 30 models in the group of near-best 3D models according to the MAD criterion for the horizontal velocity component. The magnitude range of the near-best 1D models is mostly below 1.5 mm yr^{-1} with the greatest uncertainty seen in the central part of the United States, between 30°N and 45°N , and across Baffin Island (Fig. S12c). The greatest uncertainty in the direction of horizontal velocities, that is the largest range of azimuths, is found in the northern half of the continent. Between the Great Lakes and the east coast of North America there is significant uncertainty in both the direction and magnitude of the GIA signal, reflecting uncertainty in the modelled position and extent of the collapsing peripheral bulge, where horizontal motion is predicted to peak. There is a similar situation in the northernmost part of Canada. The magnitude range of the near-best 3D GIA models shows values up to 2 mm yr^{-1} towards the west coast, where the GNSS sites have been excluded due to high tectonic activity. Similar to the situation in Europe, the 3D models show a larger range in velocity directions than the 1D models. The range in velocity directions for the 3D models is over 270° for most of the continent. The smallest range in directions is found to the west of Lake Winnipeg and across the Laurentian Plateau, which is the area where the best 1D model predicts the smallest horizontal velocities.

Table 4. Preferred properties of near-best GIA models in each category. \emptyset denotes no preference.

		Global	Europe	North America	Antarctica
1D Vertical	Lithosphere	\emptyset	\emptyset	\emptyset	\emptyset
	Upper mantle η (0.3, 0.5 or 0.8×10^{21} Pa s)	mostly smaller	smaller	\emptyset	smaller
	Lower mantle η (5, 10 or 20×10^{21} Pa s)	\emptyset	mostly smaller	mostly smaller	\emptyset
	Ice model	ICE-6G	ICE-6G	ICE-6G	ICE-6G
1D Horizontal	Lithosphere	120 km	120 and 96 km	weak preference for 120 km	\emptyset
	Upper mantle η (0.3, 0.5 or 0.8×10^{21} Pa s)	\emptyset	smaller	larger	mostly larger
	Lower mantle η (5, 10 or 20×10^{21} Pa s)	smaller	mostly small	\emptyset	\emptyset
	Ice model	\emptyset	ICE-6G	weak preference for ICE-6G	\emptyset
3D Vertical	Grain size	1 and 4 mm	4 and 10 mm	10 mm	1 mm
	Water content	\emptyset	dry	dry	wet
	Mantle model	\emptyset	\emptyset	\emptyset	\emptyset
	Ice model	\emptyset	\emptyset	\emptyset	\emptyset
3D Horizontal	Grain size	1 and 4 mm	\emptyset	weak preference for 4 mm	1 or 4
	Water content	\emptyset	dry	\emptyset	mostly dry
	Mantle model	\emptyset	S40RTS	SL	\emptyset
	Ice model	\emptyset	\emptyset	\emptyset	\emptyset

The best 1D GIA model is 6G_120p810 and the best 3D GIA model is 5G_S_dry_4mm, considering the horizontal component of velocity across North America. Figs 8(c) and (d) show residual horizontal velocities at GNSS sites across North America using these models. GNSS uncertainties are less than 0.5 mm yr^{-1} in the horizontal component for the majority of sites. There is a small number of sites with large residuals which at the same time show small uncertainties. They are almost exclusively located in the Caribbean islands and around the Gulf of Mexico. Residual vertical velocities for these sites (not shown) are also large. This region is thought to be outside the area affected by GIA and the large residuals are likely due to local effects (Milne & Peros 2013) which are not within the scope of this study. For the remaining sites south of 45°N , residual magnitudes are well below 1 mm yr^{-1} . North of 45°N , residual magnitudes are mostly between 1 and 2 mm yr^{-1} with a few sites with magnitudes up to 3 mm yr^{-1} . Along the Hudson Bay coast and in NW Canada, residuals for both models point southwards. In Newfoundland by the Labrador Sea, residuals for the 3D model point north, and residuals for the 1D model point west and southwest. Horizontal residuals for the 1D model are typically $\sim 0.5 \text{ mm yr}^{-1}$ smaller than those for the 3D model across most of North America.

4.2.3 Antarctica

Figs 7(e) and (f) show the range of horizontal GIA velocities for our near-best 1D and 3D Antarctic GIA models (six models each). Unlike in the vertical component, where we found that no 1D GIA model improves the MAD compared with the null-GIA case (*cf.* Table 1), correcting the horizontal component for GIA, using both 1D and 3D models, does reduce the MAD. The range of horizontal magnitudes (Figs 7e and S12e) for our near-best 1D models is largest near Pine Island Glacier and in the southern Weddell Sea. The magnitude range for 3D models (Figs 7f and S12f) is largest south of the Ronne Ice Shelf and on the coast east of the Ross Ice Shelf. These areas have better GNSS coverage than areas that display large uncertainty in the vertical component of GIA (*cf.* Fig. 9), raising the possibility that significant insight can be gained by comparing GIA predictions with horizontal GNSS velocities. Across most of Antarctica, the range of the horizontal GIA predictions is similar to the magnitude of the horizontal GNSS uncertainty (or rather the combined uncertainty of the elastic component and GNSS). Among the 1D models, the directions of velocities in East Antarctica do not significantly differ. The range of directions is larger in West Antarctica, with the greatest differences seen along the coast of the Amundsen Sea and in the region of the Ronne Ice Shelf. As for Europe and North America, the near-best 3D models show a much

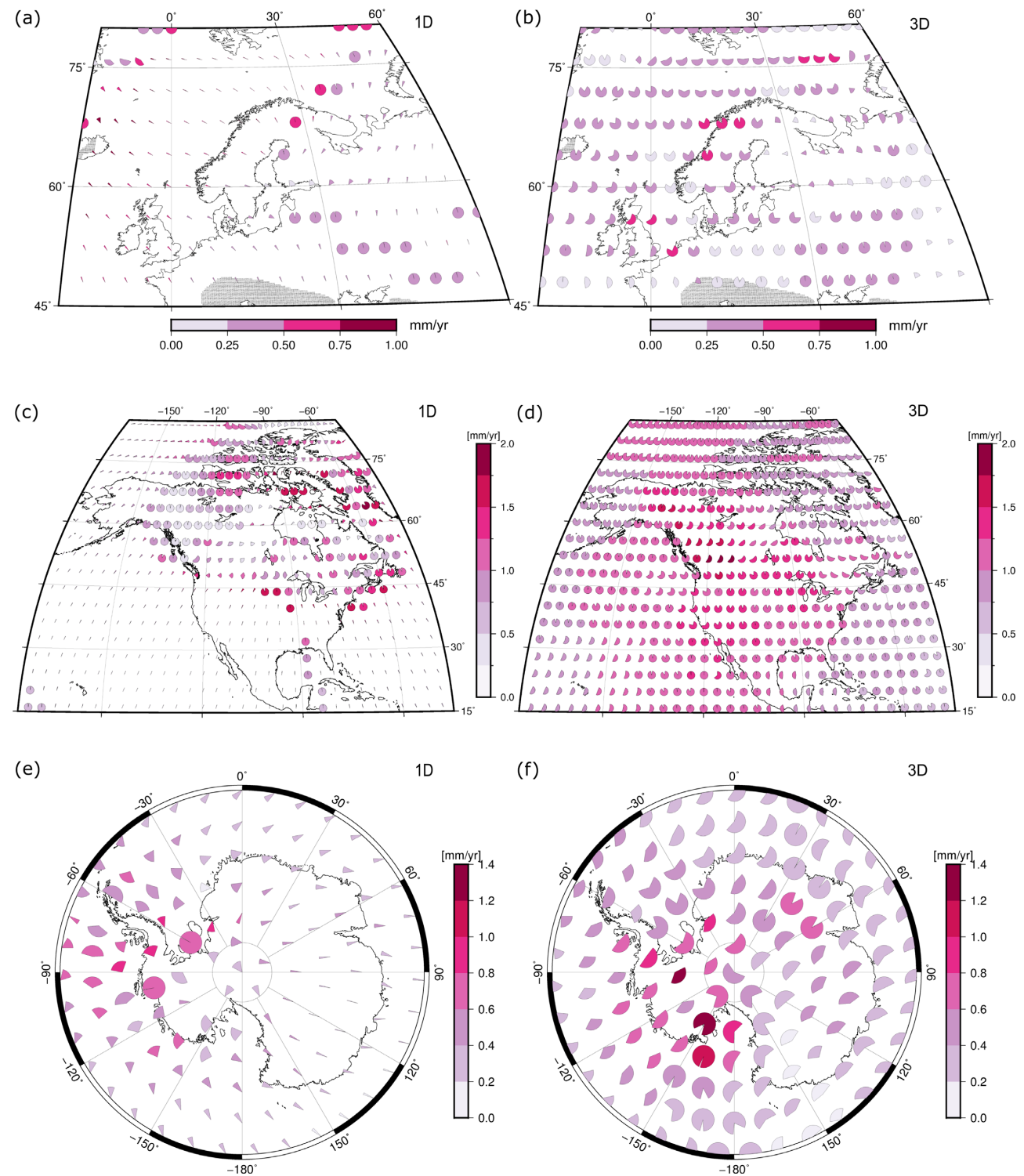


Figure 7. The colour of the pie wedges represents the range of magnitudes and the sides of the pie wedges represent the maximum and minimum azimuths of horizontal GIA predictions for models in the group of near-best 1D GIA models (left) and near-best 3D GIA models (right) for Europe (top row), North America (middle row) and Antarctica (bottom row) (*cf.* Table 2).

larger range of directions than the near-best 1D models. In some areas of East Antarctica and around the Ross Ice Shelf, the range of azimuths is well over 180° . Overall, the group of near-best 3D GIA models has larger uncertainty in both the magnitude and direction of horizontal GIA compared with the near-best 1D GIA models. It is worth noting that the magnitudes of the near-best 3D GIA models

are smaller than those of the near-best 1D GIA models, likely due to the assumption of low mantle viscosity beneath West Antarctica in the 3D GIA models, which promotes more rapid relaxation towards equilibrium. Among the group of near-best 1D models, all of them are based on ICE-6G, whereas among the near-best 3D models, they are based on ICE-6G (4 models) and W12 (2 models).

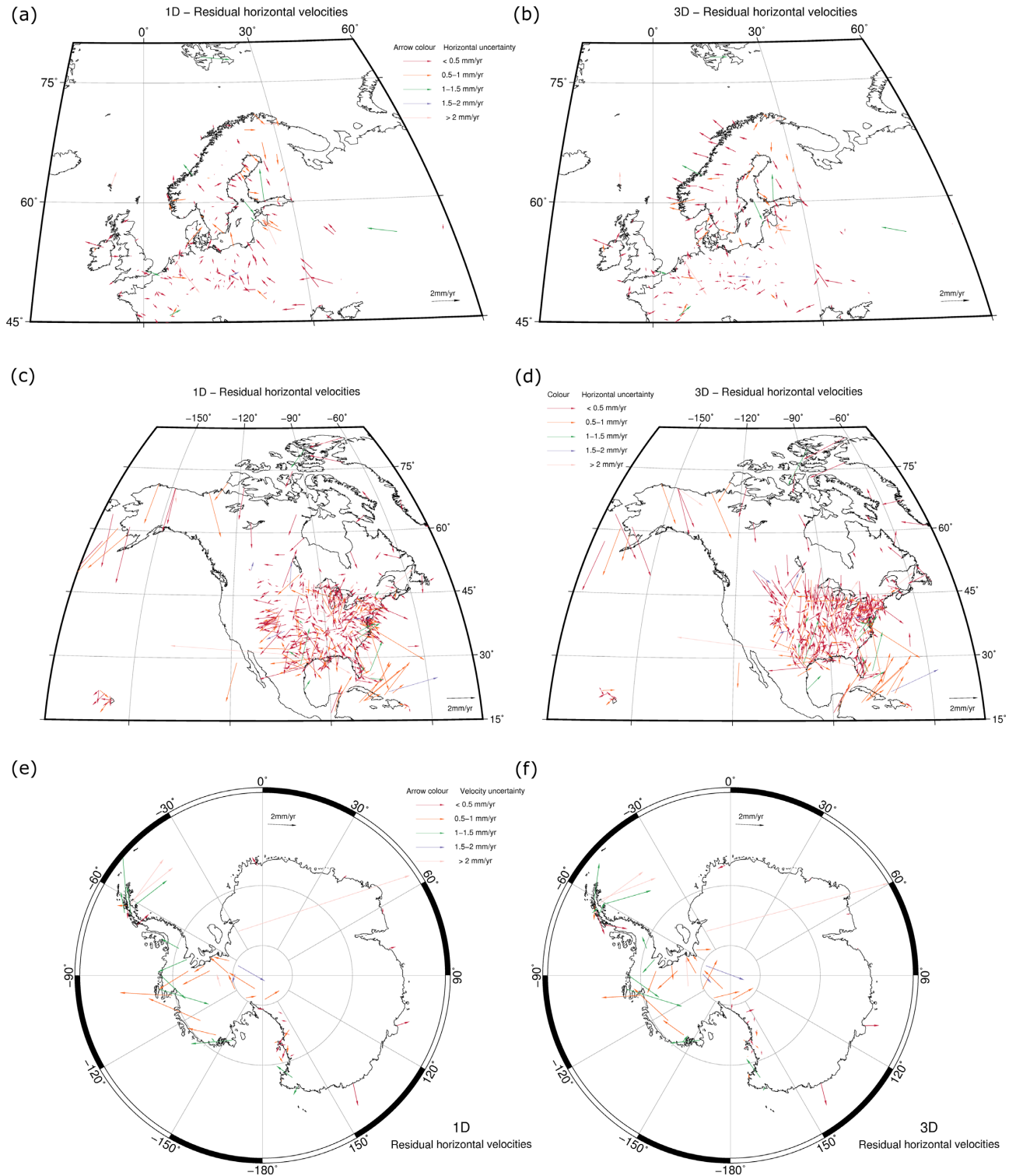


Figure 8. Residual horizontal velocity field at GNSS sites after removing plate motion and GIA using the best GIA model in the horizontal component (left column: best 1D GIA model, right column: best 3D GIA model) according to MADs for the respective region (top Europe, middle North America and bottom Antarctica). Note that for Antarctica the elastic rebound correction is also removed. The GNSS horizontal uncertainties are colour coded by magnitude according to the legends.

The best 1D GIA model in the horizontal component for Antarctica is 6G_71p85 and the best 3D GIA model is 6G_S_dry_4mm. Figs 8(e) and (f) show residual horizontal velocities in Antarctica (GIA, PMM and elastic deformation removed from the GNSS velocity field) for these models. The residual magnitudes are similar

for the two models (see also Fig. S13), showing values mostly below 1 mm yr^{-1} in East Antarctica and up to 4.1 mm yr^{-1} in West Antarctica. Around 80°S , some sites show significantly larger residual magnitudes for the 3D model than for the 1D model. Both models show the largest residuals at the tip of the Antarctic Peninsula

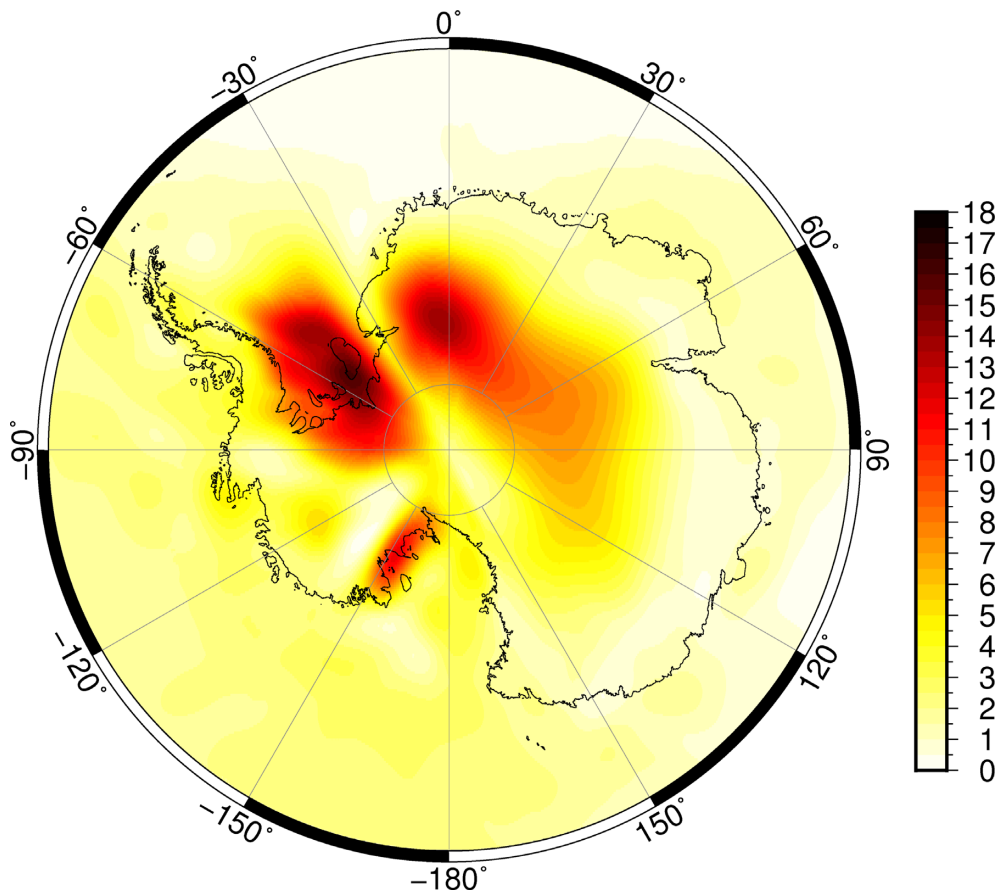


Figure 9. The uncertainty of GIA models in Antarctica in mm yr^{-1} of equivalent water height (EWH).

and on the coast by the Amundsen Sea, likely due to the fact that post-2 ka ice mass change in these regions (Nield *et al.* 2012, 2014; Barletta *et al.* 2018) is not represented in the ice history models used here. Among the residuals at the tip of the Antarctic Peninsula ($0.5\text{--}4.0 \text{ mm yr}^{-1}$), the larger residuals also have large horizontal GNSS uncertainties, and they point in the same direction for both the 1D and the 3D model. In general, the directions of the residual velocities for the 1D and 3D models are similar. Along the Transantarctic Mountains, on the Ross Sea coast, we find the smallest horizontal GNSS uncertainties in Antarctica but also the smallest residuals, with magnitudes of mostly up to 0.6 mm yr^{-1} and 0.4 mm yr^{-1} for the best 1D and 3D model, respectively. There is a tendency for the residuals of the best 3D model to be slightly smaller in this region. The best 3D GIA model predicts horizontal velocities pointing towards the Ross Sea, opposite to the best 1D model and the expected direction of deformation (which is outwards from the centre of the Last Glacial Maximum ice load). This surprising result may be explained by the findings of Hermans *et al.* (2018), who show that the direction of horizontal GIA velocities may point towards or away from a previously glaciated region, depending on the mantle viscosity.

The uncertainty of GNSS measurements across Antarctica varies, from below 0.5 mm yr^{-1} to over 2 mm yr^{-1} . The correction that must be applied to account for the elastic response to contemporary ice mass change is also subject to uncertainty. Given these issues, and the fact that the total number of Antarctic sites in our network is only 55, it remains challenging to use GNSS to test GIA models here.

5 DISCUSSION

5.1 The effect of GIA on plate motion model estimates

It is common to empirically estimate geodetic PMMs using a surface velocity field. However, horizontal surface velocities observed by GNSS do not only reflect plate motion, with the second-most influential contributor away from plate boundaries being GIA. Ideally, after correcting the GNSS surface velocity field using a GIA model, we should obtain a PMM free of GIA. However, in reality, GIA model imperfections will affect the PMM estimate. We have sought to minimize the effect of GIA on PMM estimates and we have focused our analysis on a suite of near-best GIA models.

As a result of our outlier analysis (Section 3.2.3), some sites in the northernmost part of North America were excluded in nearly all our PMM estimates. This is unfortunate because it is an area sparsely covered by GNSS sites and it means that across a large portion of the tectonic plate, the PMM estimate is not well constrained. The most likely reason that these sites were excluded is because the GIA models do not accurately estimate GIA-related motion in this region. Even after correcting for GIA, the site velocities were flagged as outliers when seeking to fit a PMM. This may be either because the plate model could not fit the residual horizontal velocities well or because the residual vertical motion was too large.

We have followed a similar approach to Booker *et al.* (2014) in creating PMMs. Booker *et al.* (2014) created a GNSS velocity field from IGS repro1 GNSS solutions aligned to the ITRF2005 reference frame and corrected it using two GIA models. In addition

to our use of a more accurate and more dense GNSS velocity field, the results obtained here are superior to the ones from Booker *et al.* (2014) in terms of the uncertainty of the Euler vector estimates (*cf.* Fig. 6) and the number of GIA models considered. Booker *et al.* (2014) corrected their GNSS velocity field using only two 1D GIA models (those of Schotman *et al.* 2008, using a modified ICE3G ice history) and a null model. They found very little variation in their estimated Euler poles, corresponding to less than $\pm 1 \text{ mm yr}^{-1}$ difference in computed plate velocities at GNSS sites. They also noted that the goodness of fit at GNSS sites improved in the vertical component with the introduction of both GIA models, but not in the horizontal. This may be because the Schotman *et al.* (2008) GIA models predict relatively small horizontal GIA velocities, due to the use of a flat Earth model, and hence applying the GIA correction had little effect on the horizontal GNSS velocities. Booker *et al.* (2014) suggest extending their analysis to include 3D GIA models. In our study, we show that the residual velocity fields created with a new suite of GIA models, including 3D GIA models, can improve the horizontal goodness of fit and influence the estimated Euler poles and plate velocities.

Taking the published ITRF2014 PMM (Altamimi *et al.* 2017) as a reference, our 3D GIA PMMs result in Euler poles closer to the ITRF2014 PMM Euler poles than the 1D GIA PMMs. The ITRF2014 PMM approach sought to minimise the effect of GIA by excluding sites with vertical velocities $\geq 0.75 \text{ mm yr}^{-1}$. The fact that our 3D GIA PMM Euler pole estimates (which consider sites in GIA regions) are close to the ITRF2014 PMM Euler pole estimates (which do not consider sites in GIA regions) indicates that the 3D GIA models used here provide a fairly accurate representation of the GIA motion that can contaminate PMM estimates.

In Antarctica, plate velocities derived using the ITRF2014 PMM are more similar to those of our 1D GIA PMMs than our 3D GIA PMMs. However, Altamimi *et al.* (2017) used sites in Antarctica regardless of whether they are in GIA-affected regions, and they did not apply a GIA correction. This, coupled with the small number of sites used, means that Antarctic tectonic plate motion in the ITRF2014 PMM is likely to be significantly affected by GIA.

Both our GIA-corrected PMMs and the ITRF2014 PMM may be considered to be affected by errors related to GIA, the former due to the choice of GIA model, the latter due to the methods used to exclude sites in GIA regions. The ITRF2014 PMM approach only excluded sites based on a vertical velocity threshold. This led to sites being retained in the regions surrounding areas of former ice loading, where GIA significantly affects the horizontal velocity field. Thus, while an agreement of our GIA PMMs with the ITRF2014 PMM can be taken as a heuristic quality measure, our GIA PMMs are preferred because the GIA effect is treated more rigorously. The method we have used allows us to include sites in GIA regions when estimating PMMs. Our results indicate that using a new suite of GIA models to correct for GIA allows us to use a larger data set when estimating PMMs, including sites in GIA-affected areas that were omitted from previous analysis because they were insufficiently well described by GIA models.

The significant variability in the Euler vectors and plate velocities associated with our GIA PMMs shows that there can be significant GIA-related horizontal motion which might be absorbed into the plate motion model if left uncorrected, even in areas that could be considered to be outside of GIA regions. A comparable result was found by Kleemann *et al.* (2008). Unlike this study, where we estimate absolute PMMs from 3D GNSS velocity fields where GIA has been removed, Kleemann *et al.* (2008) calculated the apparent incremental rotation of tectonic plates induced by modelled GIA,

considering both 1D and 3D Earth models. Their results indicate that GIA has a non-negligible effect on models of plate motion, even when considering sites at some distance from formerly glaciated areas, in agreement with our findings. This may be due to the fact that GIA models permit horizontal stresses to be transmitted long distances through the elastic lithosphere without dissipating, or it may be related to the drag exerted by the relaxing mantle on the base of the lithosphere. Both factors mean that GIA has a relatively coherent, that is plate-like, impact on far-field horizontal motion.

5.2 GIA model uncertainty

There is no consensus on how to compute the uncertainty of a GIA model. One approach is to calculate the misfit between a GIA model prediction and a set of observations. This study is an example of such an approach. However, misfits do not always reflect errors in the GIA model, other reasons for misfits include errors in the observations (in this case GNSS), and the presence of other geophysical processes contributing to vertical and horizontal deformation. Deriving reliable formal uncertainties for GIA models is a challenging task. Tarasov *et al.* (2012) attempt to quantify the uncertainty associated with the ice model component of a GIA model but they also note critical unquantified uncertainties associated with the climate forcing, deglacial ice margin chronology and Earth rheology.

In a recent publication, Simon & Riva (2020) investigate four methods of estimating GIA uncertainties: (1) parameter variation, (2) residual analysis, (3) the use of a canonical ± 20 per cent value and (4) (semi-)empirical estimation. They find that all four methods perform in a roughly consistent manner, making them all potentially suitable for uncertainty estimation. However, they find that the ± 20 per cent rule may underestimate uncertainties in the centre of former ice sheets and be inappropriate for application in far-field regions and regional studies. They also find that the parameter variation method may be overly pessimistic for 1D GIA models and note that it would be difficult to apply to models that implement 3D Earth structure due to the larger number of free parameters.

In this paper, the range of GIA predictions produced by our near-best models may be regarded as a measure of the uncertainty of the GIA models. This is comparable to a combination of the above-mentioned methods of Simon & Riva (2020): (1) parameter variation and (2) residual analysis. Here, parameter variation is considered only for groups of ‘realistic’ GIA models selected by validation with GNSS observations. Our method is comparable with that of Vestøl *et al.* (2019) who also use GNSS observations to help quantify GIA uncertainties. Specifically, Vestøl *et al.* (2019) compare the output from 11 025 different GIA models with GNSS uplift rates and precise levelling, and compute the standard deviation of a subset of 21 ‘good’ GIA models.

We formed groups of near-best models, separately considering 1D and 3D GIA models, as well as vertical and horizontal velocity components (Tables 2 and B2–B5). The near-best models are chosen based on their MAD values, and the variation of models within these groups is considered to be an indication of uncertainty in the GIA estimate. Simon & Riva (2020) state that the disadvantage of the parameter variation approach is that it may give unrealistically large uncertainty estimates, particularly in load centres, and that the selection of which parameters to vary is itself subject to uncertainty. The advantage of the approach taken in this paper is that the group of GIA models is also validated against empirical data. It is important

to stress, however, that our approach does not provide a formal statistical measure of GIA modelling uncertainty.

Quantification of GIA uncertainty is important because when estimating surface mass change from satellite gravity missions, such as GRACE and GRACE Follow-On, the GIA signal component must be accounted for (e.g. King *et al.* 2012a; Velicogna & Wahr 2013; Caron *et al.* 2018). The uncertainty associated with the GIA signal contributes to the uncertainty of the surface mass change estimates. This is particularly interesting for Antarctica, which is still covered in ice. In order to estimate present-day ice mass changes from gravity, the gravity change caused by GIA-related deformation must be removed. The range of vertical GIA predictions for our near-best (3D) GIA models in Antarctica can be interpreted as an uncertainty measure of GIA across Antarctica, and Fig. 9 shows these uncertainties expressed in mm yr^{-1} equivalent water height (EWH). In this estimate, the rock density is taken to be 3700 kg m^{-3} (Wahr *et al.* 2000; Riva *et al.* 2009). The uncertainty associated with GIA reaches several mm yr^{-1} EWH across most of Antarctica. The largest uncertainties are found in the area of the Ronne Ice Shelf (up to 18 mm yr^{-1} EWH), inland of Dronning Maud Land, East Antarctica (up to 14 mm yr^{-1} EWH) and at the grounding line of the Ross Ice Shelf (up to 12 mm yr^{-1} EWH).

The GIA vertical predictions can also be expressed as an equivalent annual mass change value for the whole region, which can be interpreted as the GIA contribution to observed annual mass change from the GRACE (and Follow-On) missions. We consider Antarctica as a whole (Antarctic Ice Sheet, AIS) and divided into three areas: the West Antarctic Ice Sheet (WAIS), East Antarctic Ice Sheet (EAIS) and Antarctic Peninsula (AP). We use the boundaries defined by Zwally *et al.* (2012) and account for the smoothing required when interpreting GRACE data by applying a 400 km Gaussian filter and extending each area with a buffer zone of 200 km. The contribution of GIA to annual mass change for each ice sheet area is quantified using each of our near-best 3D GIA models. There is no group of near-best 1D GIA models because, for the vertical component, none of the 1D GIA models had a smaller MAD value than the null-GIA case. The results are listed in Table 5. Over the AIS, depending on which GIA model from the group of near-best models is used, the predicted GIA contribution to observed annual mass change ranges from -3.26 to 22.11 Gt yr^{-1} (*cf.* Table 5). As mentioned in Section 3.3.2, near-best models are nearly as good as the best model and the best model cannot be distinguished from the near-best models in the sense that any of them could have been the best model if a different GNSS data set had been used. However, statistically 5G_S_wet_1mm is shown to be the best among them. Values from this model can be used to represent the contribution of GIA to mass change in each of the domains considered, while the range of predictions among the near-best models (far-right-hand column Table 5) represents the uncertainty of the GIA models. The uncertainty for the whole of the AIS is equivalent to $\sim 25 \text{ Gt yr}^{-1}$.

Shepherd *et al.* (2018) analyse the mass balance of Antarctica for the 1992–2017 period using a range of satellite observations. They find ice-mass change rates of $5 \pm 46 \text{ Gt yr}^{-1}$ for the EAIS, $-94 \pm 27 \text{ Gt yr}^{-1}$ for the WAIS and $-20 \pm 15 \text{ Gt yr}^{-1}$ for the AP. For the whole of Antarctica, Shepherd *et al.* (2018) find a rate of $-109 \pm 56 \text{ Gt yr}^{-1}$. Using ten GIA models that cover all of Antarctica, they find that the GIA-induced mass change estimates are in relatively good agreement, ranging from 12 Gt yr^{-1} to 81 Gt yr^{-1} , with a mean value of 56 Gt yr^{-1} . Their low-end estimate of 12 Gt yr^{-1} is based on the only model in their study that accounts for lateral variations in Earth rheology, and thus it is the most comparable to our estimates in Table 5, which are also based on 3D GIA model outputs.

The GIA model uncertainties (ranges) that we report in Table 5 are approximately half the value of the ice mass change uncertainties reported in Shepherd *et al.* (2018), with the exception of the AP where our values are approximately a third of theirs. Gunter *et al.* (2014) report mass change estimate uncertainties which fall between the value of ours and those of Shepherd *et al.* (2018). The above may indicate that our results contribute to a narrowing of GIA-related uncertainties in GRACE mass estimates for Antarctica. However, Shepherd *et al.* (2018)'s and Gunter *et al.* (2014)'s confidence limits reflect total uncertainty (which also accounts for other error sources) unlike ours which only reflect GIA-related uncertainty, so it is unsurprising that our values are lower.

The range of velocity azimuths predicted by a suite of GIA models (Fig. 7) represents the uncertainty in the direction of GIA-related horizontal deformation. In each of our three regions of interest (Europe, North America and Antarctica), the range of azimuths for the near-best 3D GIA models is larger than the range of azimuths for the near-best 1D GIA models. The near-best 1D GIA models in the horizontal component are all based on ICE-6G, whereas among the near-best 3D GIA models, there is a larger variety in ice models. To investigate whether the larger variation in horizontal azimuths among the 3D GIA models, compared with the 1D GIA models, is due to different ice models, the azimuths were also inspected for a subset of near-best 3D GIA models created using the same ice model. A large range of azimuths was still observed, suggesting that the predicted horizontal velocities are very sensitive to lateral variations in mantle viscosity, in agreement with Kaufmann *et al.* (2005).

5.3 GIA and PMM model fit to the GNSS velocity field

In this study we seek an optimum global GIA model which, when combined with its accompanying plate motion model, best explains the global surface velocity field as determined by GNSS observations. Considering the 117 GIA models investigated in this study, the best global 3D GIA model for each velocity component has a smaller plate-weighted MAD than the best 1D GIA model for that component (*cf.* Table 1). In the horizontal component for the global case, none of the 1D GIA models are better than the null-GIA case, whereas multiple 3D GIA models are better than the null-GIA case in both horizontal and vertical components. This suggests that 3D Earth structure is important when seeking to replicate the global horizontal velocity field. In Antarctica, none of the 1D GIA models fit the GNSS vertical velocity field better than the null-GIA case, whereas several 3D GIA models show an improvement of the fit. In North America and Europe, the 1D GIA models give a better fit in the vertical component than the 3D GIA models. One of the reasons for this could be the fact that the ice models used here were developed assuming 1D Earth structure.

Kierulf *et al.* (2014) investigate the fit of vertical and horizontal GIA model predictions to GNSS velocities in Fennoscandia using an alternative approach where they express the GNSS velocities in a so-called ‘GIA reference frame’. They transform the GNSS velocities to a reference frame defined by each GIA model using a four-parameter similarity transformation, where only the three elements of the rotation matrix and the scale rate parameter are estimated. The disadvantage of their method is that it introduces more degrees of freedom, might increase uncertainty, and potentially masks large scale systematic GIA model biases. Compared to a traditional approach, where the reference frame is fixed and rigid plate motion is removed, the advantage of their method is that it

Table 5. GIA contribution to annual mass change in Antarctica using each of the near-best GIA models, and the uncertainty (range) in mass change due to GIA. Shown for the WAIS, EAIS, AP and Antarctica as a whole (AIS). GIA models with smallest to largest MAD values are listed from left to right. All values are in Gt yr^{-1} .

Gt yr^{-1}	5G_S_wet_1mm	W12_SL_dry_1mm	W12_SL_wet_1mm	6G_SL_wet_1mm	Range of mass change estimates
WAIS	3.52	17.38	1.99	2.47	15.39
EAIS	14.63	1.45	-4.98	19.89	24.86
AP	0.86	4.48	0.44	0.72	4.04
AIS	17.54	15.96	-3.26	22.11	25.37

avoids the influence of errors in scale, rotation, geocentre position, and plate motion on the comparison between the GNSS velocity field and the GIA model. However, their approach can only be applied in regional studies within one tectonic plate since it would otherwise be contaminated by rigid plate motion. In the present study, the residual velocities for each GIA model are compared without contamination by an external PMM and after correcting for frame origin differences. A set of PMMs is estimated from a bespoke GNSS surface velocity field corrected with a set of GIA models. Differences in reference frame origins, rigid plate motion and the GNSS network are taken into consideration. Therefore, our approach is an alternative to the ‘GIA reference frame’ approach of Kierulf *et al.* (2014) and we expect it to be able to better constrain and test global GIA models.

6 CONCLUSIONS

We created a global surface velocity field, ‘NCL20’, using time series of reprocessed GNSS measurements. The GNSS velocity field was corrected for GIA using a suite of GIA models and used to estimate global plate motion models. We used a set of 1D and 3D GIA models which has not previously been compared with horizontal GNSS rates. Each global PMM was used to estimate plate velocities and differences in frame origins (β'), and the related GIA model predictions were removed from the GNSS velocity field to obtain a residual velocity field (Fig. 1 summarises our approach). The residual velocity field was used to validate the GIA models. Obtaining the velocity field and estimating plate models has been carried out with thorough attention to error sources and the exclusion of outliers. Unlike regional model-data comparisons where relatively simple methods can be applied to remove errors due to the reference frame, this study offers a global approach. The GNSS networks are well-aligned to the ITRF2014 reference frame and the variations of reference frame origins between the different velocities (GIA, GNSS and plate velocities) are taken into account in the PMM estimates and the computation of the residuals.

A set of PMMs was created using both the raw GNSS velocity field (GNSS-only PMM) and the surface velocity field corrected with various GIA predictions (1D GIA PMMs and 3D GIA PMMs). From these PMMs, a subset of ‘near-best’ PMMs and their associated GIA models was further analysed. The best and near-best GIA models are chosen according to their MAD (Median Absolute Deviation) values, and the ranking of the PMM is based on the ranking of the GIA model that was used in estimating that PMM. Our work resulted in the following conclusions:

(i) Our network combination method has enabled the creation of a dense global velocity field with improved coverage in the GIA affected regions of North America, Europe and Antarctica [compared

to, e.g. Booker *et al.* (2014), the IGS network Rebischung *et al.* (2016) or the ITRF network Altamimi *et al.* (2016)].

(ii) It is shown that using an extensive set of 1D and 3D GIA models facilitates the estimation of a PMM from a larger and therefore more robust GNSS data set, compared with previous global PMM estimates where sites in GIA regions had to be removed.

(iii) GIA-related horizontal motion may be incorporated into plate motion if left uncorrected. This can significantly influence plate velocities on the millimetre level. This is important for North America and Europe which have areas that are affected by GIA, and especially Antarctica where almost the entire plate is affected by GIA.

(iv) Compared with the 1D GIA PMMs, our 3D GIA PMM Euler poles are located closer to the ITRF2014 PMM Euler poles (derived by excluding sites in GIA regions). This suggests that 3D GIA models may be better than 1D GIA models at correcting for horizontal GIA motion, which can bias PMM estimates. We note that GIA PMMs and the ITRF2014 PMM may both be considered to be affected by errors related to GIA, the former due to the choice of GIA model, the latter due to the methods used to exclude sites in GIA regions. Still, the agreement of a GIA PMM with the ITRF2014 PMM can be taken as an indication that the GIA model provides a reasonable estimate of GIA at sites excluded in the ITRF2014 PMM. An advantage of our approach is that GIA is treated rigorously, considering both the horizontal and vertical components of deformation.

(v) Our PMM estimates for Antarctica in this paper include ~ 8 times more sites than the ITRF2014 PMM and also result in a significant reduction of the Euler vector uncertainty (formal error) for this plate.

(vi) When validating GIA models with GNSS observations, jointly seeking a GIA model-PMM combination that minimizes the residual surface velocity field is preferable to using a (pre-existing) PMM, which may be contaminated by GIA. Additionally, the joint estimation takes into consideration differences in frame origins between the GIA model, GNSS network, and rigid plate motion model, further improving the residuals.

(vii) The globally best-fitting PMM estimated here (Table 3), is a state-of-the-art geodetic PMM which may be used in other studies that seek to investigate tectonic plate motion or require correction for plate motion.

(viii) The subsets of suitable GIA models presented here, that is the near-best models (*cf.* Tables B2–B5), may be used in crustal deformation studies where a correction for GIA is required. Furthermore, the ranges of the GIA model predictions selected here may be interpreted as a measure of GIA model uncertainty, and can contribute to error budgeting.

(ix) In each of the three regions of interest (Europe, North America and Antarctica), the range of azimuths of near-best 3D GIA

models is larger than the range of azimuths of near-best 1D GIA models.

(x) The range of Antarctic vertical motions encompassed by the allowable (i.e. near-best) GIA models is equivalent to a range of Antarctic mass changes from -3 Gt yr^{-1} to 22 Gt yr^{-1} . This range is smaller than the confidence limits of some present-day mass balance estimates and represents a lower bound on the likely uncertainty associated with the GIA correction that must be applied when using gravimetry to estimate ice mass balance.

ACKNOWLEDGMENTS

KV was funded by a studentship from the UK Natural Environment Research Council (NERC) ‘IAPETUS’ Doctoral Training Partnership and by the School of Engineering, Newcastle University. PJC acknowledges support from NERC grants NE/J005789/1, NE/R002029/1 and NE/K004085/1. PLW acknowledges support from NERC fellowship NE/K009958/1, and grants NE/R002029/1 and NE/K003674/1. We would like to thank Wouter van der Wal for providing the 3D GIA code and Glenn Milne for providing the 1D GIA code. We would like to thank Volker Klemann and an anonymous reviewer for their helpful comments.

DATA AVAILABILITY

The bulk of the GNSS data underlying this paper are available from the EUREF Permanent GNSS Network (http://www.epncb.oma.be/_productsservices/analysiscentres/combosolframe.php), IGS repositories (<ftp://ftp.igs.org/pub/center/analysis/>) and UNAVCO repositories (<ftp://data-out.unavco.org/pub/products/sinex>). The subset of suitable GIA models (near-best models) will be available in Whitehouse et al. (Pangaea, in preparation).

REFERENCES

- Altamimi, Z., Collilieux, X. & Métivier, L., 2011. ITRF2008: an improved solution of the international terrestrial reference frame, *Geophys. J. Int.*, **85**(8), 457–473.
- Altamimi, Z., Métivier, L. & Collilieux, X., 2012. ITRF2008 plate motion model, *J. geophys. Res.*, **117**(B7), doi:10.1029/2011JB008930.
- Altamimi, Z., Rebischung, P., Métivier, L. & Collilieux, X., 2016. ITRF2014: a new release of the International Terrestrial Reference Frame modeling nonlinear station motions, *Geophys. J. Int.*, **121**(8), 6109–6131.
- Altamimi, Z., Métivier, L., Rebischung, P., Rouby, H. & Collilieux, X., 2017. ITRF2014 plate motion model, *Geophys. J. Int.*, **209**(3), 1906–1912.
- Argus, D.F., Gordon, R.G., Heflin, M.B., Ma, C., Eanes, R.J., Willis, P., Peltier, W.R. & Owen, S.E., 2010. The angular velocities of the plates and the velocity of Earth’s centre from space geodesy, *Geophys. J. Int.*, **180**(3), 913–960.
- Argus, D.F., Gordon, R.G. & DeMets, C., 2011. Geologically current motion of 56 plates relative to the no-net-rotation reference frame, *Geochem. Geophys. Geosyst.*, **12**(11), doi:10.1029/2011GC003751.
- Baarda, W., 1968. *A Testing Procedure for Use in Geodetic Networks*, Publications on Geodesy Vol. 2(Nr. 5), Netherlands Geodetic Commission.
- Barletta, V.R. et al., 2018. Observed rapid bedrock uplift in Amundsen Sea Embayment promotes ice-sheet stability, *Science*, **360**(6395), 1335–1339.
- Bastos, L., Bos, M. & Fernandes, R.M., 2010. Deformation and tectonics: contribution of GPS measurements to plate tectonics - overview and recent developments, in *Sciences of Geodesy – I*, pp. 155–184, ed. Xu, G., Springer, doi:10.1007/978-3-642-11741-1_5.
- Bevis, M. et al., 2009. Geodetic measurements of vertical crustal velocity in West Antarctica and the implications for ice mass balance, *Geochem. Geophys. Geosyst.*, **10**(10), doi:10.1029/2009GC002642.
- Bird, P., 2003. An updated digital model of plate boundaries, *Geochem. Geophys. Geosyst.*, **4**(3), doi:10.1029/2001GC000252.
- Blewitt, G., 2003. Self-consistency in reference frames, geocenter definition, and surface loading of the solid Earth, *J. geophys. Res.*, **108**(B2), doi:10.1029/2002JB002082.
- Blewitt, G., Kreemer, C., Hammond, W.C. & Gazeaux, J., 2016. MIDAS robust trend estimator for accurate GPS station velocities without step detection, *J. geophys. Res.*, **121**(3), 2054–2068.
- Bock, Y. & Melgar, D., 2016. Physical applications of GPS geodesy: a review, *Rep. Prog. Phys.*, **79**(10), 106801, doi:10.1088/0034-4885/79/10/106801.
- Booker, D., Clarke, P.J. & Lavallée, D.A., 2014. Secular changes in Earth’s shape and surface mass loading derived from combinations of reprocessed global GPS networks, *J. Geod.*, **88**(9), 839–855.
- Booker, D.P.A., 2012. Secular changes in Earth’s shape and surface mass loading, *PhD thesis*, University of Newcastle upon Tyne, School of Civil Engineering and Geosciences.
- Caron, L., Ivins, E.R., Larour, E., Adhikari, S., Nilsson, J. & Blewitt, G., 2018. GIA model statistics for grace hydrology, cryosphere, and ocean science, *Geophys. Res. Lett.*, **45**(5), 2203–2212.
- Chase, C.G., 1978. Plate kinematics: the Americas, East Africa, and the rest of the world, *Earth planet. Sci. Lett.*, **37**(3), 355–368.
- Coulson, S., Lubeck, M., Mitrovica, J.X., Powell, E., Davis, J.L. & Hoggard, M.J., 2021. The Global fingerprint of modern ice-mass loss on 3D crustal motion, *Geophys. Res. Lett.*, **48**(16), doi:10.1029/2021GL095477.
- Cross, P.A., 1992. *Advanced Least Squares Applied to Position-Fixing*, University of East London, Working Paper No. 6, ISSN:0260-9142.
- Davies, P. & Blewitt, G., 2000. Methodology for global geodetic time-series estimation: a new tool for geodynamics, *J. geophys. Res.*, **105**(B5), 11 083–11 100.
- Davies, P. B.H., 1997. Assembling the IGS Polyhedron, *PhD thesis*, School of Civil Engineering and Geosciences, University of Newcastle upon Tyne.
- DeMets, C., Gordon, R., Argus, D. & Stein, S., 1990. Current plate motions, *Geophys. J. Int.*, **101**, 425–478.
- DeMets, C., Gordon, R.G., Argus, D.F. & Stein, S., 1994. Effect of recent revisions to the geomagnetic reversal time scale on estimates of current plate motions, *Geophys. Res. Lett.*, **21**(20), 2191–2194.
- DeMets, C., Gordon, R.G. & Argus, D.F., 2010. Geologically current plate motions, *Geophys. J. Int.*, **181**(1), 1–80.
- Dziewonski, A.M. & Anderson, D.L., 1981. Preliminary reference Earth model, *Phys. Earth planet. Inter.*, **25**(4), 297–356.
- Fowler, C. M.R., 2005. *The Solid Earth: An Introduction to Global Geophysics*, 2nd edn, Cambridge Univ. Press.
- Griffiths, J., 2019. Combined orbits and clocks from IGS second reprocessing, *J. Geod.*, **93**, 177–195.
- Gunter, B.C., Didova, O., Riva, R. E.M., Ligtenberg, S. R.M., Lenaerts, J. T.M., King, M.A., van den Broeke, M.R. & Urban, T., 2014. Empirical estimation of present-day Antarctic glacial isostatic adjustment and ice mass change, *Cryosphere*, **8**(2), 743–760.
- Hermans, T. H.J., van der Wal, W. & Broerse, T., 2018. Reversal of the direction of horizontal velocities induced by GIA as a function of mantle viscosity, *Geophys. Res. Lett.*, **45**(18), 9597–9604.
- Hirth, G. & Kohlstedt, D., 2003. Rheology of the upper mantle and the mantle wedge: a view from the experimentalists, *Wash. DC Am. Geophys. Un. Geophys. Monogr. Ser.*, **138**, 83–105.
- Karato, S.-I., 2008. *Deformation of Earth Materials: An Introduction to the Rheology of Solid Earth*, Cambridge Univ. Press.
- Kaufmann, G., Wu, P. & Ivins, E.R., 2005. Lateral viscosity variations beneath Antarctica and their implications on regional rebound motions and seismotectonics, *J. Geodyn.*, **39**(2), 165–181.
- Kendall, R.A., Mitrovica, J.X. & Milne, G.A., 2005. On post-glacial sea level-II. Numerical formulation and comparative results on spherically symmetric models, *Geophys. J. Int.*, **161**(3), 679–706.
- Kierulf, H.P., Plag, H.-P., Kristiansen, O. & Nørbech, T., 2003. *Towards the True Rotation of a Rigid Eurasia*, EUREF Publication 12, pp. 118–124.
- Kierulf, H.P., Steffen, H., Simpson, M. J.R., Lidberg, M., Wu, P. & Wang, H., 2014. A GPS velocity field for Fennoscandia and a consistent comparison

- to glacial isostatic adjustment models, *J. geophys. Res.*, **119**(8), 6613–6629.
- Kierulf, H.P., Steffen, H., Barletta, V.R., Lidberg, M., Johansson, J., Kristiansen, O. & Tarasov, L., 2021. A GNSS velocity field for geophysical applications in Fennoscandia, *J. Geodyn.*, **146**, 101845 , doi:10.1016/j.jog.2021.101845.
- King, M., Bingham, R., Moore, P., Whitehouse, P., Bentley, M. & Milne, G., 2012a. Lower satellite-gravimetry estimates of Antarctic sea-level contribution, *Nature*, **491**, 586–589.
- King, M.A. *et al.*, 2010. Improved constraints on models of glacial isostatic adjustment: a review of the contribution of ground-based geodetic observations, *Surv. Geophys.*, **31**(5), 465–507.
- King, M.A., Keshin, M., Whitehouse, P.L., Thomas, I.D., Milne, G. & Riva, R.E.M., 2012b. Regional biases in absolute sea-level estimates from tide gauge data due to residual unmodeled vertical land movement, *Geophys. Res. Lett.*, **39**(14) , doi:10.1029/2012GL052348.
- King, M.A., Whitehouse, P.L. & van der Wal, W., 2015. Incomplete separability of Antarctic plate rotation from glacial isostatic adjustment deformation within geodetic observations, *Geophys. J. Int.*, **204**(1), 324–330.
- Klemann, V., Martinec, Z. & Ivins, E.R., 2008. Glacial isostasy and plate motion, *J. Geodyn.*, **46**(3), 95–103.
- Koch, K.-R., 1999. *Parameter Estimation and Hypothesis Testing in Linear Models*, Springer-Verlag.
- Kreemer, C., Blewitt, G. & Klein, E.C., 2014. A geodetic plate motion and Global Strain Rate Model, *Geochem. Geophys. Geosyst.*, **15**(10), 3849–3889.
- Lambeck, K., Rouby, H., Purcell, A., Sun, Y. & Sambridge, M., 2014. Sea level and global ice volumes from the last glacial maximum to the Holocene, *Proc. Natl. Acad. Sci. U.S.A.*, **111** , doi:10.1073/pnas.1411762111.
- Lambeck, K., Purcell, A. & Zhao, S., 2017. The North American Late Wisconsin ice sheet and mantle viscosity from glacial rebound analyses, *Quater. Sci. Rev.*, **158**, 172–210.
- Larson, K.M., Freymueller, J.T. & Philipsen, S., 1997. Global plate velocities from the Global Positioning System, *J. geophys. Res.*, **102**(B5), 9961–9981.
- Lavallée, D.A., 2000. Tectonic plate motions from global GPS measurements, *PhD thesis*, Department of Geomatics, University of Newcastle upon Tyne.
- Lavallée, D.A., 2006. *The Tanya Software, Tanyak version 1.6*, Newcastle University.
- Lowrie, W., 2007. *Fundamentals of Geophysics*, Cambridge Univ. Press.
- Melini, D., Gegout, P., Spada, G. & King, M.A., 2014. REAR—A Regional ElAstic Rebound Calculator.
- Métivier, L., Altamimi, Z. & Rouby, H., 2020. Past and present ITRF solutions from geophysical perspectives, *Adv. Space Res.*, **65**, 2711–2722.
- Milne, G.A. & Peros, M., 2013. Data-model comparison of Holocene sea-level change in the circum-Caribbean region, *Global Planet. Change*, **107**, 119–131.
- Minster, J.B. & Jordan, T.H., 1978. Present-day plate motions, *J. geophys. Res.*, **83**(B11), 5331–5354.
- Mitrovica, J.X. & Milne, G.A., 2003. On post-glacial sea level—I. General theory, *Geophys. J. Int.*, **154**(2), 253–267.
- Mitrovica, J.X., Milne, G.A. & Davis, J.L., 2001. Glacial isostatic adjustment on a rotating earth, *Geophys. J. Int.*, **147**(3), 562–578.
- Nield, G.A., Whitehouse, P.L., King, M.A., Clarke, P.J. & Bentley, M.J., 2012. Increased ice loading in the Antarctic Peninsula since the 1850s and its effect on glacial isostatic adjustment, *Geophys. Res. Lett.*, **39**(17) , doi:10.1029/2012GL052559.
- Nield, G.A. *et al.*, 2014. Rapid bedrock uplift in the Antarctic Peninsula explained by viscoelastic response to recent ice unloading, *Earth planet. Sci. Lett.*, **397**, 32–41.
- Peltier, W.R., 2004. Global glacial isostasy and the surface of the Ice-Age Earth: the ICE-5G (VM2) model and GRACE, *Ann. Rev. Earth Planet. Sci.*, **32**(1), 111–149.
- Peltier, W.R., Argus, D.F. & Drummond, R., 2015. Space geodesy constrains ice age terminal deglaciation: the global ICE-6G_C (VM5a) model, *J. geophys. Res.*, **120**(1), 450–487.
- Plag, H.-P. & Pearlman, M., 2009. *Global Geodetic Observing System: Meeting the Requirements of a Global Society on a Changing Planet in 2020*, Springer-Verlag.
- Plag, H.-P., Nørbech, T. & Kristiansen, O., 2002. Effects of intraplate deformations on fixing regional reference frames, in *EUREF Publication No. 10*, Vol. **23**, pp. 118–124, eds Torres, J. A. & Hornik, H., Verlag des Bundesamtes.
- Rebisching, P., Altamimi, Z., Ray, J. & Garayt, B., 2016. The IGS contribution to ITRF2014, *J. Geod.*, **90**, 611–630.
- Ritsema, J., Deuss, A., van Heijst, H.J. & Woodhouse, J.H., 2011. S40RTS: a degree-40 shear-velocity model for the mantle from new Rayleigh wave dispersion, teleseismic traveltimes and normal-mode splitting function measurements, *Geophys. J. Int.*, **184**(3), 1223–1236.
- Riva, R.E. *et al.*, 2009. Glacial Isostatic Adjustment over Antarctica from combined ICESat and GRACE satellite data, *Earth planet. Sci. Lett.*, **288**(3), 516–523.
- Schaeffer, A.J. & Lebedev, S., 2013. Global shear speed structure of the upper mantle and transition zone, *Geophys. J. Int.*, **194**(1), 417–449.
- Schotman, H. & Vermeersen, L., 2005. Sensitivity of glacial isostatic adjustment models with shallow low-viscosity earth layers to the ice-load history in relation to the performance of GOCE and GRACE, *Earth planet. Sci. Lett.*, **236**(3), 828–844.
- Schotman, H., Wu, P. & Vermeersen, L., 2008. Regional perturbations in a global background model of glacial isostasy, *Phys. Earth planet. Inter.*, **171**(1), 323–335.
- Schumacher, M., King, M.A., Rougier, J., Sha, Z., Khan, S.A. & Bamber, J.L., 2018. A new global GPS data set for testing and improving modelled GIA uplift rates, *Geophys. J. Int.*, **214**(3), 2164–2176.
- Sen, P.K., 1968. Estimates of the regression coefficient based on Kendall's tau, *J. Am. Stat. Assoc.*, **63**(324), 1379–1389.
- Shepherd, A. *et al.*, 2018. Mass balance of the Antarctic Ice Sheet from 1992 to 2017, *Nature*, **558** , doi:10.1038/s41586-018-0179-y.
- Shepherd, A. *et al.*, 2019. Trends in Antarctic ice sheet elevation and mass, *Geophys. Res. Lett.*, **46**(14), 8174–8183.
- Šídák, Z., 1967. Rectangular confidence regions for the means of multivariate normal distributions, *J. Am. Stat. Assoc.*, **62**(318), 626–633.
- Simon, K.M. & Riva, R.E.M., 2020. Uncertainty estimation in regional models of long-term GIA uplift and sea level change: an overview, *J. geophys. Res.*, **125**(8), doi:10.1029/2019JB018983.
- Tanaka, Y., Klemann, V., Martinec, Z. & Riva, R.E.M., 2011. Spectral-finite element approach to viscoelastic relaxation in a spherical compressible Earth: application to GIA modelling, *Geophys. J. Int.*, **184**(1), 220–234.
- Tarasov, L., Dyke, A.S., Neal, R.M. & Peltier, W., 2012. A data-calibrated distribution of deglacial chronologies for the North American ice complex from glaciological modeling, *Earth planet. Sci. Lett.*, **315–316**, 30–40.
- Teunissen, P., 2017. Batch and Recursive Model Validation, in *Springer Handbook of Global Navigation Satellite Systems*, pp. 687–720, eds Teunissen, P. & Montenbruck, O., Springer International Publishing.
- Theil, H., 1950. A rank-invariant method of linear and polynomial regression analysis, *Indagationes Mathematicae*, **12**, 85–91.
- Thomas, I.D. *et al.*, 2011. Widespread low rates of Antarctic glacial isostatic adjustment revealed by GPS observations, *Geophys. Res. Lett.*, **38**(22) , doi:10.1029/2011GL049277.
- Torge, W. & Müller, J., 2012. *Geodesy*, 4th edn, De Gruyter.
- van der Wal, W., Barnhoorn, A., Stocchi, P., Gradmann, S., Wu, P., Drury, M. & Vermeersen, B., 2013. Glacial isostatic adjustment model with composite 3D Earth rheology for Fennoscandia, *Geophys. J. Int.*, **194**(1), 61–77.
- Vardić, K., Clarke, P.J. & Whitehouse, P.L., 2021. NCL20: A global GNSS velocity field for estimating tectonic plate motion and testing GIA models, *PANGAEA - Data Publisher for Earth & Environmental Science*, doi:10.1594/PANGAEA.935079.

- Velicogna, I. & Wahr, J., 2013. Time-variable gravity observations of ice sheet mass balance: precision and limitations of the GRACE satellite data, *Geophys. Res. Lett.*, **40**(12), 3055–3063.
- Vestøl, O., Ågren, J., Steffen, H., Kierulf, H.P. & Tarasov, L., 2019. NKG2016LU: a new land uplift model for Fennoscandia and the Baltic Region, *J. Geod.*, **93**, 1759–1779.
- Wahr, J., Wingham, D. & Bentley, C., 2000. A method of combining ICESat and GRACE satellite data to constrain Antarctic mass balance, *J. geophys. Res.*, **105**(B7), 16279–16294.
- Whitehouse, P.L., 2009. Glacial isostatic adjustment and sea-level change: state of the art report, Technical Report, Svensk Kärnbränslehantering, Stockholm, ISSN:1404-0344.
- Whitehouse, P.L., 2018. Glacial isostatic adjustment modelling: historical perspectives, recent advances, and future directions, *Earth Surf. Dyn.*, **6**(2), 401–429.
- Whitehouse, P.L., Bentley, M.J., Milne, G.A., King, M.A. & Thomas, I.D., 2012. A new glacial isostatic adjustment model for Antarctica: calibrated and tested using observations of relative sea-level change and present-day uplift rates, *Geophys. J. Int.*, **190**(3), 1464–1482.
- Zwally, H.J., Giovinetto, M.B., Beckley, M.A. & Saba, J.L., 2012. Antarctic and Greenland Drainage Systems, Internal report, GSFC Cryospheric Sciences Laboratory, at: https://icesat4.gsfc.nasa.gov/cryo_data/ant_grn_drainage_systems.php.

SUPPORTING INFORMATION

Supplementary data are available at [GJI](#) online.

Figure S1. Suspected outliers (marked in magenta) of the PMM based on the GNSS-only velocity field. Grey denotes sites that were included in the final PMM estimate.

Figure S2. Euler pole locations for Eurasia tectonic plate. See Fig. 4 in the main text for location in world map.

Figure S3. Euler pole locations for the North America tectonic plate. See Fig. 4 in the main text for location in world map.

Figure S4. Euler pole locations for Antarctica tectonic Plate. See Fig. 4 in the main text for location in world map.

Figure S5. Plate velocities on Eurasia Plate estimated with best 1D GIA PMM and best 3D GIA PMM and the differences between those and the ones estimated with near-best 1D GIA PMM and near-best 3D GIA PMM, respectively. Note the difference in scale.

Figure S6. Plate velocities on Eurasia Plate estimated with best 1D and 3D GIA PMMs and the differences between those and the ones estimated with GNSS-only PMM and ITRF2014 PMM. Note the difference in scale.

Figure S7. Plate velocities on North America plate estimated with best 1D and 3D GIA PMM and the differences between those and the ones estimated with near-best 1D and 3D GIA PMMs, respectively. Note the difference in scale.

Figure S8. Plate velocities on North America Plate estimated with best 1D and 3D GIA model and the differences between those and the ones estimated with a plate model estimated with GNSS-only PMM and the ITRF2014 PMM. Note the difference in scale.

Figure S9. Plate velocities on Antarctica Plate estimated with best 1D and 3D GIA model and the differences between those and the ones estimated with models from groups of near-best 1D and 3D models, respectively. Note the difference in scale.

Figure S10. Plate velocities on Antarctica Plate estimated with best 1D and 3D GIA PMM and the differences between those and the ones estimated with GNSS-only PMM and ITRF2014 PMM. Note the difference in scale.

Figure S11. Vertical (top) and horizontal (bottom) elastic rebound due to present-day ice mass changes at GNSS sites in Antarctica.

Figure S12. The maximum difference between horizontal magnitudes of GIA predictions for models in the group of near-best 1D GIA models (left column) and near-best 3D GIA models (right column) for Europe (top row), North America (middle row) and Antarctica (bottom row). The shaded areas cover high tectonic strain regions where the GNSS sites have been disregarded. Circles represent network GNSS sites. Supplement to Fig. 7 in the main text.

Figure S13. Magnitudes of the residual horizontal velocity field at GNSS sites after removing plate motion and GIA using the best GIA model for the respective region according to MADs in the horizontal component (top Europe, middle North America, bottom Antarctica): the best 1D GIA model (left) and the best 3D GIA model (right).

Table S1. The XYZ components of the estimated vector β' (in mm yr^{-1}) which represents the sum of the geocentre origin rate bias and the velocity of the reference frame in which the relevant GIA model is expressed with respect to CM, for each PMM. See Section 3.2.1. for details.

Please note: Oxford University Press is not responsible for the content or functionality of any supporting materials supplied by the authors. Any queries (other than missing material) should be directed to the corresponding author for the paper.

APPENDIX A: ESTIMATING A SURFACE VELOCITY FIELD

A1 Input GNSS networks

The solutions we used are the operational solutions from the stated IGS Analysis Centres (ACs, cf. Section 2.1) and the solutions from the IGS repro2 campaign. The end dates of repro2 generally correspond to the time when an AC updated their operational processing to repro2 standards (Griffiths 2019). From GPS week 1832 (February 2015), the IGS officially switched their operational solutions to using the same antenna calibrations and analysis methods as in repro2; the exact GPS weeks for individual ACs are shown in Fig. A1. From GPS week 1934 (29th January 2017), the IGS has switched to using different antenna calibrations (igs14.atx), hence for consistency, the time series in our solution ends there.

A2 Network combination

The network combination is performed using the Newcastle University-developed reference frame combination software Tanya (Davies 1997; Lavallée 2006; Booker 2012).

A2.1 Deconstraining

When solving for coordinate parameters in a geodetic network, additional constraint information is added to the observations to define the network's reference system parameters (Davies 1997). The daily epoch solutions from the ACs introduced in Section A1 are provided as constrained solutions, and in this paper we deconstrained them to obtain free-network solutions. Free-network solutions are independent of an external reference frame and AC-specific constraining techniques, which makes them more suitable for creating a combined network. In Tanya, deconstraining is performed in the stochastic domain, in two steps: (1) removing constraints stated in the given *a priori* solution and (2) removing unstated minimum constraints (Davies & Blewitt 2000).

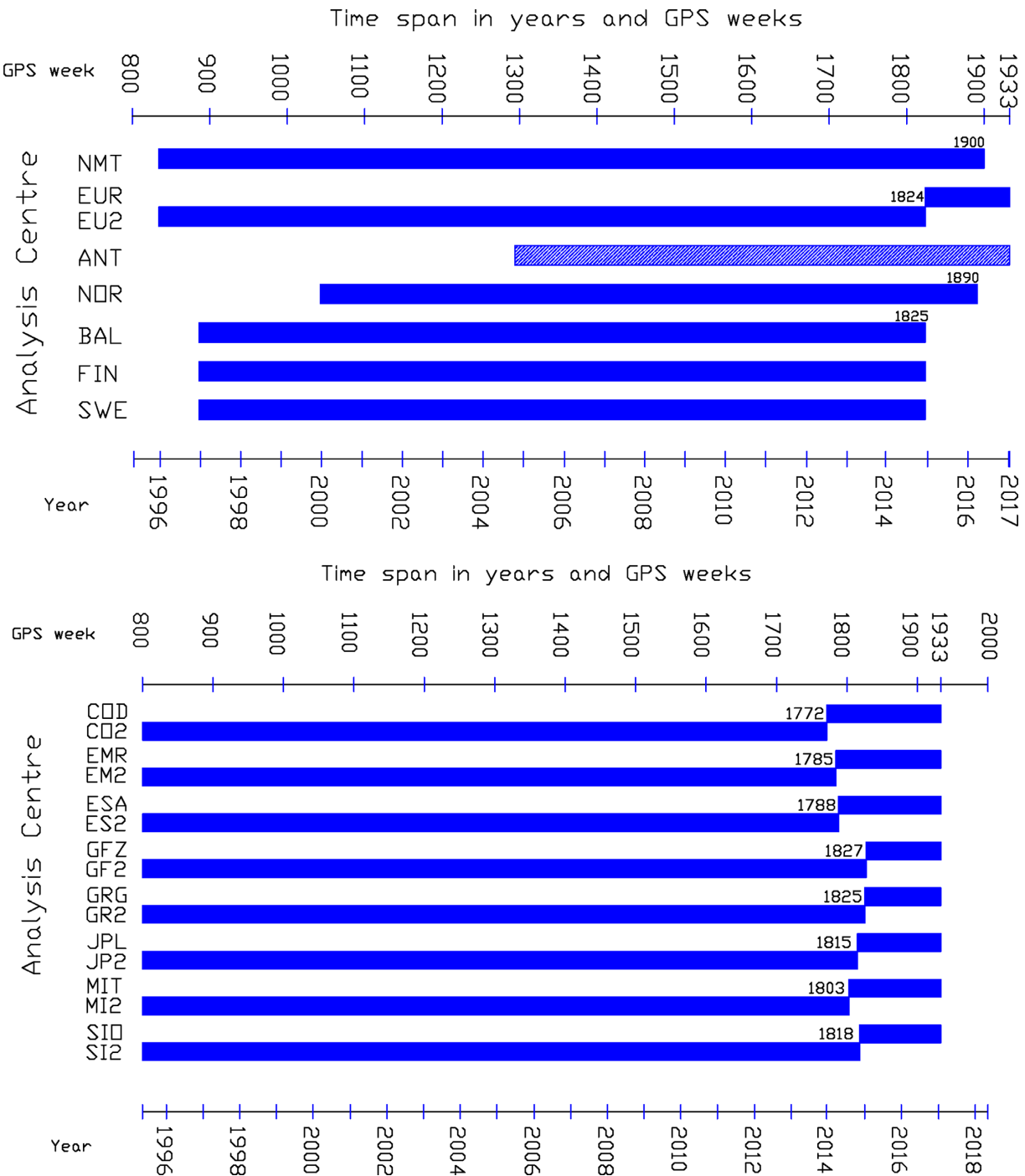


Figure A1. Global IGS ACs (bottom) and regional ACs (top) used in the present network combination and their respective time spans. Numbers associated with a shift in the timeline denote the week for which the AC finished their repro2 analysis and started processing operational solutions in the same way. ANT data span exhibits a large data gap of ~ 2 yr from 2010 to 2012.

A2.2 Combining and aligning epoch solutions

We combined multiple epoch solutions and aligned them to the ITRF2014 reference frame. Aligning here means estimating transformation parameters between a network and a reference network through a chosen set of mutual sites and applying the estimated transformation parameters to the former network, in order to express it in the reference frame of the latter one. To express each combined daily solution in the ITRF2014 reference frame (i.e. align each combined daily solution to ITRF2014), a reference network

in the respective epoch and reference frame is needed. The reference networks for alignment were obtained by propagating the ITRF2014-IGS kinematic solution to the epochs of the daily solutions in the time series. A kinematic solution contains positions for a specific epoch in time and velocities for determining positions in any later epoch. To propagate ITRF2014-IGS to the desired epoch, appropriate sets of positions, velocities and variance-covariance matrices (VCMs) valid for the respective epoch need to be chosen. Once we chose the appropriate parameters, we computed the

Table A1. IGS ACs whose products were used in the present network combination.

Full name of AC	Operational solution ID / abbreviation of AC	Repro2 solution ID
Centre for Orbit Determination Europe	COD	CO2
Natural Resources Canada	EMR	EM2
European Space Agency	ESA	ES2
GeoForschungsZentrum	GFZ	GF2
Groupe de Recherche en Géodésie Spatiale	GRG	GR2
Jet Propulsion Laboratory	JPL	JP2
Massachusetts Institute of Technology	MIT	MI2
Scripps Institute of Technology	SIO	SI2

position of the site in ITRF2014-IGS at the relevant epoch. In the most simple case of a kinematic solution with linear velocity, the position in the propagation epoch is computed using the velocity and the time difference between the reference and propagation epoch, according to:

$$X_t = X_0 + \dot{X} \cdot \Delta t, \quad (\text{A1})$$

where X_0 is the position of a site at reference epoch t_0 , X_t is the position of a site at time t , Δt is the time that passed since the reference epoch t_0 until t and \dot{X} is the linear velocity of the site. For sites for which post-seismic deformation (PSD) models (Altamimi *et al.* 2016) are available, the non-linear site displacement caused by post-seismic relaxation is also computed and the position is corrected for it.

Global epoch network solutions are combined in an iterative process creating combined global networks. Due to computational costs, regional solutions are later attached to the combined global solutions. Once the global solutions are deconstrained, a block scaling factor (BSF) is applied to their VCMs. This determines the influence that each network has on the final combined solution. We apply it because the relative scaling of the input AC network VCMs is not always correct (Davies & Blewitt 2000), some ACs may state overly optimistic or overly pessimistic VCMs of their solutions in comparison to the other ACs. The BSFs were determined empirically through consecutive daily network combinations with the idea of following long-term trends in AC networks' matrix scaling and solution performance (Davies 1997).

In the usual Tanya network combination, sites are included only if they appear in three or more AC solutions. This was changed in this study to provider a denser network suitable for testing GIA models, by including any site which is processed by at least one of the ACs in the combined network. The global networks were combined within the least-squares framework using the step-by-step least squares method (e.g. Cross 1992). Reduced normal equations are formed and outliers are removed using data snooping (Baarda 1968). The normal equations are stacked (summed) and solved, giving a loose combined global daily network.

Finally, each loose combined network was aligned to ITRF2014 using a 7-parameter Helmert transformation between the loose daily combined network and the ITRF2014 network propagated to the corresponding day. We estimated the Helmert parameters in an iterative process. Thus, an automatic procedure was introduced to exclude sites that show inconsistencies between the epoch solutions and the propagated ITRF2014, which would distort the network through suboptimal Helmert transformation parameters.

The estimated Helmert parameters were then applied to all the sites in the network. This transforms the combined daily network solution reference frame into ITRF2014. The weighted root mean square error (WRMS) of the alignment of the combined network

with ITRF2014-IGS is ~ 2.5 mm on average. The time series is shown in Fig. A2.

A2.3 Network combination discussion

The operational solutions for GPS weeks 1832–1933 (15th February 2015 – 28th January 2017) use equivalent GNSS processing standards to repro2. We computed the WRMS of the operational Newcastle University GNAAC solutions (using the previous version of Tanya with alignment to ITRF2008 reference frame; obtained from the IGS report archive at <https://lists.igs.org/pipermail/igsreport/>). That combination differs from the one in this paper in the reference frame and network combination methodology, but uses the same input AC solutions. We then compared the WRMS values of the two solutions (Fig. A2) in their overlapping period (GPS weeks 1832–1933). We found that the solutions from this paper reduce the WRMS by 57 per cent on average (from 8.0 mm to 3.5 mm).

Each of the daily regional solutions is deconstrained as described above and the loose solution is aligned to the global combined solution at each day. EUR, NMT and ANT are aligned to the combined global solution directly. To increase the number of common sites for network alignment, we aligned the Fennoscandian and Baltic networks (BAL, FIN, SWE and NOR) to EUR, which we had previously aligned to the combined solution. The Helmert parameters are estimated in an iterative process as for the global solutions. Finally, we obtain a global set of daily positions in ITRF2014 reference frame. The sites have time spans of up to 20 years (Fig. A1).

A3 Velocity estimation

For the velocity estimation, we used the Median Interannual Difference Adjusted for Skewness (MIDAS), a trend estimator introduced by Blewitt *et al.* (2016). MIDAS is based on the Theil-Sen (Theil 1950; Sen 1968) estimator. In the case of coordinate time series, the ordinary Theil-Sen is defined as the median of slopes between all possible pairs of data. MIDAS restricts the pairs to those separated by one year, which mitigates seasonality and minimizes the fraction of pairs that span discontinuities.

In the original MIDAS algorithm, if for a certain position record in the time series, a suitable pair is not found which is exactly one year apart, the next available position record is taken regardless of how far apart in time they are. Here, we enhanced the MIDAS algorithm by additionally including a tolerance value for the deviation from one year. In our version, if two data points separated by exactly one year cannot be found, the algorithm searches for a pair that is within a 'tolerance value' before or after the one year difference. We tested tolerance values of 1 week to 4 weeks, with the upper limit chosen to avoid seasonal signals. We found that the difference in velocity estimates with 1 week, 2 weeks, 3 weeks and 4 weeks

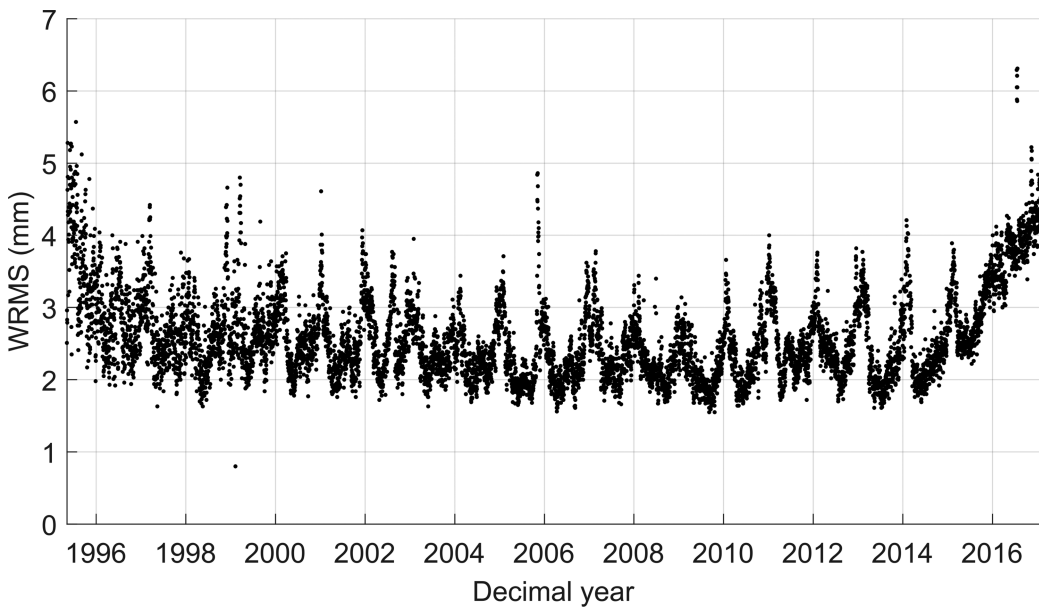


Figure A2. WRMS of the post-fit residuals of the alignment of the combined global network to ITRF2014.

tolerance value is lower than the uncertainty estimate and finally chose 4 weeks to maximise the amount of usable data.

A3.1 Time series analysis

The MIDAS trend estimator works on one velocity component at a time and therefore cannot take into consideration any correlation between the coordinate components (Blewitt *et al.* 2016). To mitigate the correlation between components when estimating the trend, we do this in the topocentric East-North-Up (ENU) reference system which by the nature of GNSS is far less correlated than the geocentric (XYZ) components. For each site we compute coordinate differences of positions with respect to a reference position (chosen to be the median of all positions in the site's time series) and convert these coordinate differences and their uncertainties to the ENU system. Before estimating the trend, we performed a three-step refining and filtering of the sites and individual positions' records, as follows:

- (i) Exclude sites in high tectonic strain areas.
- (ii) Exclude position records with high position uncertainties.
- (iii) Examine position records which show anomalies.

(1) Sites in high tectonic strain areas are excluded because they would contaminate the GIA and rigid plate motion study. The sites in high and low tectonic strain areas were selected using the Global Strain Rate Model (Kreemer *et al.* 2014) by interpolating the strain values to our network sites and choosing only sites where the second invariant of the strain tensor was smaller than 0.1 microstrains. Additionally, sites which are within 100 km of high tectonic strain areas are excluded. Fig. A3 shows the resulting sites in low tectonic strain areas.

(2) MIDAS uses the median to estimate the trend which means that it does not take into consideration the formal errors of individual positions. By visual inspection of the spread of position uncertainties, we consider position records to be reliable for velocity estimation when σ_E and σ_N are within 10 mm and σ_U is within 15 mm, as the large majority of records lie well within these values.

(3) Within the remaining data in the time series, we exclude the records of coordinate differences (with respect to the reference position) larger than 100 m, as these only appear as a small number of individual records (maximum 20 daily records per site in entire time series) that cannot represent a step discontinuity but only outliers. We then investigate the coordinate differences between 1 m and 100 m which could not be due to any credible long term displacement. We found that nearly all sites have less than 0.01 per cent of such records per site, which are easily detected as outliers by the MIDAS median estimator in the trend estimate. The remaining sites (namely AUS1, SMM1 and SMM2) which have a large proportion of records with coordinate differences between 1 m and 100 m were analysed manually and remained in the data set at this step.

We estimated site velocities for each of the networks — the global combined network and the aligned regional networks. We gave priority to higher-order networks when a site was estimated in multiple networks, for example a global network site estimate is prioritised over a regional network site estimate, and EUREF sites over Fennoscandian and Baltic sites. The velocity field consists of 1218 sites which are then further subjected to quality control.

A4 Excluding sites from the velocity field

To ensure that the velocity field is not biased by multiple site estimates in a small area, we removed such duplicate sites. Sites which are within 100 m are likely to be the same site, but situated on different monuments. We selected groups of sites that are within 100 m radius from each other and merged them if their velocities were similar. The merged site gets a new name, that is a new four-character SITE ID code, starting with the first three characters of the names of the merging sites followed by 'M'. If the velocities within 100 m were not similar, the site with the smallest velocity uncertainty was chosen. Monuments are usually within tens of metres from each other. Thus, if sites are more than 100 m and less than 5 km from each other, this is likely not the same site and in that case, we chose the site with the smallest velocity uncertainty.

To remove outliers, that is sites which seem to show movements that are beyond what could be explained by any natural long term

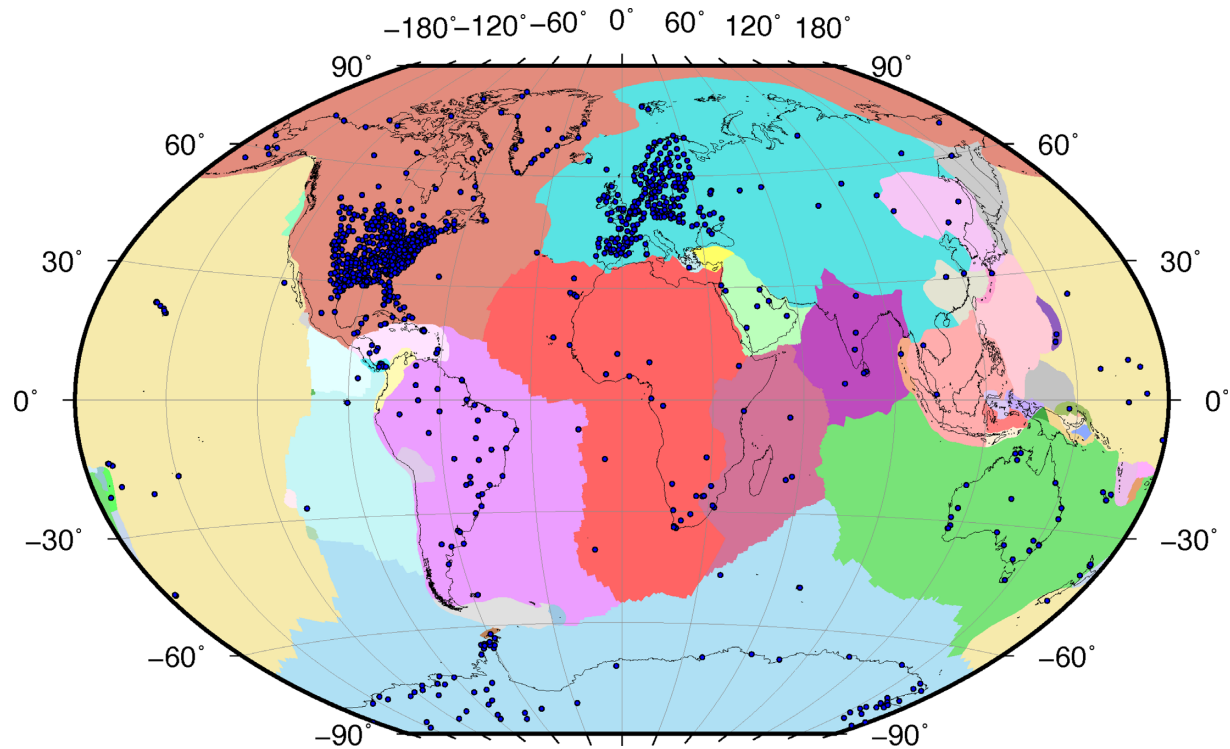


Figure A3. Tectonic plate boundaries from Bird (2003) and sites in low tectonic strain areas.

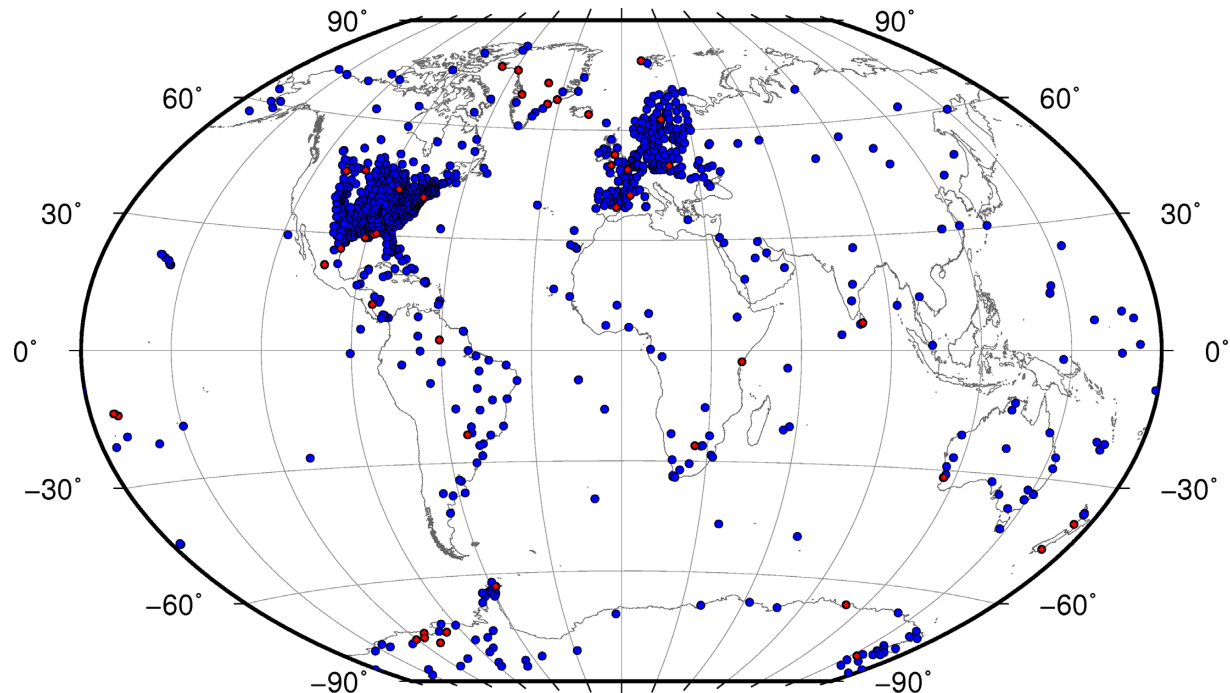


Figure A4. Remaining (blue) and excluded (red) sites depending on whether the site velocities are larger than the threshold based on the GIA range and GNSS uncertainty. See text for details.

tectonic or GIA displacement, we chose a threshold based on the overall range of GIA models at that site. The threshold for the vertical component is the sum of (1) the range of GIA models vertical predictions plus (2) an additional 50 per cent of the range as a safety measure, plus (3) the 3σ formal uncertainty of the GNSS velocity component. The threshold for the horizontal component is the sum of (1) maximum horizontal velocity magnitude from the range of GIA models plus (2) an additional 50 per cent of that

value, plus (3) the 3σ formal uncertainty of the horizontal speed determined by GNSS. Before considering the horizontal threshold, a preliminary plate motion model estimated from GNSS velocities using the method outlined in Section 3.2 was subtracted. Any site with a velocity larger than the threshold is considered to entail velocities that cannot contribute to the study of plate motion and GIA. In this step, 47 sites are excluded (Fig. A4) which led to our final global GNSS velocity field.

APPENDIX B: ‘NEAR-BEST’ GIA MODELS

Table B2. Groups of near-best GIA models in Europe based on their MADs. The groups were formed by considering all models with MADs better than the null-GIA case and within $0.1/0.2 \text{ mm yr}^{-1}$ of the best model for the horizontal and the vertical component, respectively (*cf.* Section 3.3.2).

Groups of near-best models Europe			
Vertical 1D	6G_71p320 6G_71p310 6G_96p320 6G_96p55 W12_71p35 6G_120p55 5G_71p35 6G_96p310 6G_96p35 6G_96p520 6G_71p35 6G_120p520 6G_96p510 6G_120p820 6G_120p510 6G_120p810 6G_71p55 5G_96p35 6G_120p85 5G_71p310 6G_120p320 W12_96p35 W12_71p310 6G_71p510 W12_120p35	Vertical 3D	W12_SL_dry_4mm 5G_SL_dry_4mm 6G_SL_dry_4mm 5G_S_dry_4mm W12_S_dry_4mm 6G_S_dry_10mm 5G_S_dry_10mm 6G_S_dry_4mm W12_S_dry_10mm W12_SL_wet_10mm 5G_SL_wet_10mm 5G_SL_dry_10mm 6G_SL_dry_10mm W12_SL_dry_10mm W12_S_dry_1mm W12_SL_wet_4mm 6G_SL_dry_1mm W12_SL_dry_1mm W12_SL_dry_1mm
Horizontal 1D	6G_96p310 6G_96p35 6G_120p35 6G_120p320 6G_120p310 6G_96p320	Horizontal 3D	6G_S_dry_4mm 5G_S_dry_4mm W12_S_dry_4mm 6G_S_dry_1mm 6G_SL_dry_10mm 5G_S_dry_1mm W12_S_dry_1mm 5G_SL_dry_10mm W12_SL_dry_10mm

Table B3. Groups of near-best models in North America based on their MADs. The groups were formed as in Table B2.

Groups of near-best models North America			
Vertical 1D	6G_120p820 6G_96p820 6G_96p520 6G_120p520 6G_71p820 6G_120p810	Vertical 3D	6G_SL_dry_10mm W12_S_dry_10mm 6G_S_dry_10mm 5G_S_dry_10mm W12_SL_dry_10mm 5G_SL_dry_10mm W12_S_dry_4mm 6G_S_dry_4mm 5G_S_dry_4mm 6G_S_dry_1mm 6G_SL_dry_4mm W12_SL_dry_4mm 6G_SL_dry_1mm 5G_SL_dry_4mm 6G_S_wet_4mm W12_S_wet_10mm
Horizontal 1D	6G_120p810 6G_120p520 6G_120p85 6G_120p820 6G_120p510 6G_96p520 6G_96p85	Horizontal 3D	5G_S_dry_4mm W12_S_dry_4mm W12_SL_dry_4mm W12_SL_dry_10mm 5G_SL_dry_4mm 5G_SL_dry_10mm 6G_S_wet_4mm 5G_SL_dry_1mm W12_SL_dry_1mm W12_S_wet_4mm 5G_S_wet_10mm 6G_S_dry_4mm 5G_S_wet_4mm 6G_SL_dry_4mm W12_S_wet_10mm 6G_S_wet_10mm 6G_SL_dry_1mm 6G_SL_dry_10mm 6G_SL_wet_10mm 5G_SL_wet_4mm W12_SL_wet_4mm W12_S_wet_1mm 5G_SL_wet_10mm 6G_SL_wet_4mm 5G_S_wet_1mm 6G_S_wet_1mm 5G_S_dry_1mm W12_SL_wet_10mm W12_S_dry_1mm 6G_S_dry_1mm

Table B4. Groups of near-best models in Antarctica based on their MADs. The groups were formed as in Table B2.

Groups of near-best models Antarctica			
Vertical 1D	∅	Vertical 3D	5G_S_wet_1mm W12_SL_dry_1mm W12_SL_wet_1mm 6G_SL_wet_1mm
Horizontal 1D	6G_71p85 6G_96p820 6G_71p55 6G_120p85 6G_96p510 6G_96p810	Horizontal 3D	6G_S_dry_4mm 6G_SL_dry_4mm 6G_SL_wet_10mm W12_SL_dry_1mm 6G_SL_dry_1mm W12_S_dry_4mm

Table B5. Groups of near-best models globally based on their MADs (when weighting by plate area is applied). The groups were formed as in Table B2.

Groups of near-best models globally (plate weighted)			
Vertical 1D	6G_120p820 6G_120p320 6G_120p520	Vertical 3D	W12_SL_dry_1mm W12_S_dry_1mm 6G_S_dry_1mm 6G_SL_dry_1mm 5G_SL_dry_1mm W12_SL_wet_4mm 6G_SL_wet_4mm 6G_S_wet_4mm 6G_SL_wet_1mm 5G_S_dry_1mm W12_SL_wet_1mm W12_S_wet_4mm 6G_SL_dry_4mm 6G_SL_wet_10mm 6G_S_wet_10mm 5G_SL_wet_1mm 5G_SL_wet_4mm W12_SL_wet_10mm
Horizontal 1D	∅	Horizontal 3D	6G_SL_wet_10mm W12_S_dry_4mm 6G_S_wet_10mm 6G_SL_dry_4mm 5G_SL_wet_10mm 5G_SL_dry_4mm 5G_S_wet_10mm W12_SL_wet_10mm 6G_S_dry_4mm 6G_S_wet_1mm 5G_S_wet_1mm W12_S_wet_1mm W12_SL_dry_1mm